

Ideal Quantum Nondemolition Readout of a Flux Qubit without Purcell Limitations


Xin Wang^{1,2,*}, Adam Miranowicz^{2,3} and Franco Nori^{2,4}

¹*Institute of Quantum Optics and Quantum Information, School of Science, Xi'an Jiaotong University, Xi'an, 710049, China*

²*Theoretical Quantum Physics Laboratory, RIKEN Cluster for Pioneering Research, Wako-shi, Saitama, 351-0198, Japan*

³*Faculty of Physics, Adam Mickiewicz University, 61-614 Poznań, Poland*

⁴*Physics Department, The University of Michigan, Ann Arbor, Michigan 48109-1040, USA*

 (Received 7 August 2019; revised manuscript received 29 September 2019; published 16 December 2019)

Dispersive coupling based on the Rabi model with large detuning is widely used for qubit quantum nondemolition (QND) readout in quantum computation. However, the measurement speed and fidelity are usually significantly limited by the Purcell effects (i.e., Purcell decay, critical photon numbers) and qubit-dependent Kerr nonlinearity. To avoid these effects, we propose how to realize an ideal QND readout of a gradiometric flux qubit with a tunable gap via its nonperturbative dispersive coupling (NPDC) to a frequency-tunable measurement resonator. We show that this NPDC-based readout mechanism is free of dipole-field interactions and that the qubit QND measurement is not deteriorated by intracavity photons. Both qubit-readout speed and qubit-readout fidelity can avoid the Purcell limitations. Moreover, NPDC can be conveniently turned on and off via an external control flux. We show how to extend this proposal to a multiqubit architecture for a joint qubit readout.

DOI: [10.1103/PhysRevApplied.12.064037](https://doi.org/10.1103/PhysRevApplied.12.064037)

I. INTRODUCTION

Performing large-scale quantum computation requires fast and high-fidelity qubit readout to compete with the decoherence of fragile quantum states [1–4]. For some robust error-correction proposals (such as surface codes [5,6]), the qubit measurement also has to be repeated many times to give an accurate diagnosis of the corrections within a given coherence time [7]. In quantum computing, on the basis of circuit quantum electrodynamics [8,9], a superconducting qubit is often read out by its dispersive coupling with an auxiliary cavity [10–16]. The cavity frequency depends on the qubit state [9]. If a coherent drive is applied to the initially empty cavity near its resonance frequency, the qubit state is encoded in the output field and is obtained by distinguishing two pointer states in phase space [17].

Recently, a number of studies were devoted to quantum-information processing with flux qubits, showing the increasing usefulness of these circuits [18–24]. However, the dispersive coupling of a flux qubit is usually based on the dipole-field interaction between a resonator and a qubit, described by $H_x = g_x(a + a^\dagger)\sigma_x$ [10], with a (a^\dagger) being the annihilation (creation) operator of the cavity and

$\sigma_{x,z}$ being the Pauli operators of the qubit. In the large-detuning regime, the system Hamiltonian can be written as (hereafter we set $\hbar = 1$) [25–27]

$$H_d = \omega_r a^\dagger a + \frac{\omega_q}{2} \sigma_z + \chi_z^I \sigma_z a^\dagger a + K_I (a^\dagger a^\dagger a a) \sigma_z, \quad (1)$$

where ω_q (ω_r) is the qubit (resonator) frequency and $\chi_z^I \simeq \lambda g_x$ is the induced dispersive coupling (IDC) strength with

$$\lambda = g_x / (\omega_q - \omega_r) \ll 1. \quad (2)$$

The Kerr nonlinearity $K_I = -\lambda^3 g_x$ depends on the qubit state. The original Hamiltonian H_x does not commute with the Pauli operator σ_z , and therefore the qubit readout via H_d is not an ideal quantum nondemolition (QND) measurement [28].

The IDC sets limitations on both qubit-measurement fidelity and qubit-measurement speed. First, the homodyne-detection speed relies on a high value of the photon-escape rate κ [29,30]. However, because of virtual excitation exchange, this strong dissipation channel leads to an additional qubit Purcell decay at rate $\Gamma_p = \lambda^2 \kappa$ [29,31–33], which might destroy both gate-operation fidelity and readout fidelity (see Appendix A). One can suppress this additional decay by using a Purcell filter [30,34,35], which, however, increases experimental complexity. Second, to suppress the qubit-error transitions

*wangxin.1989@stu.xjtu.edu.cn

induced by the dipole-field interaction, the intracavity photon number $\langle a^\dagger a \rangle$ should be lower than the critical photon number $n_c = 1/4\lambda^2$ (i.e., in the quasi-QND regime) [10], which can lead to a poor pointer-state separation with a long measurement time.

All these trade-off relations result from the dipole-field interaction, which reduces the fidelity of a QND measurement. We present here a method for measuring a gradiometric flux qubit via its nonperturbative dispersive coupling (NPDC) with a frequency-tunable resonator. This mechanism results from the dispersive coupling via a longitudinal degree of freedom of the qubit, rather than from perturbation of the dipole-field interaction. Therefore, the intracavity photons cannot deteriorate the qubit QND readout, and the Purcell effects are effectively avoided. We prove that both readout fidelity and readout speed can go beyond the Purcell limitations. A recent preprint [33] has also discussed the problem of how to realize a QND measurement by using transverse couplings. However, to avoid Purcell effects, the method in Ref. [33] requires numerical optimization of various system parameters, including designing time-dependent coupling pulses of ultrashort duration. The readout channel of that method also needs to be rapidly switched on and off. All these requirements might be challenging in experiments. In contrast to that method, our proposal is based on the NPDC readout mechanism and thus it does not suffer from such limitations.

II. NONPERTURBATIVE DISPERSIVE COUPLING

As demonstrated in Fig. 1, we consider a gradiometric four-Josephson-junction (JJ) flux qubit with a tunable gap [36–40] interacting with a frequency-tunable transmission-line resonator (TLR). There are two kinds of circulating currents in the qubit: (i) the conventional persistent current I_p (red arrows) in the main loop [41–46] and (ii) the circulating current $I_{\text{cir},\alpha}$ (blue arrow) in the α loop [39,47], which is related to the longitudinal degree of freedom and was much-less discussed in previous studies [48–50]. At the optimal point, the qubit frequency ω_q is tuned by the flux Φ_α through the α loop. As discussed in Appendix C, in the Pauli-operator notation of the qubit ground-state and excited-state basis, the main-loop current operator is $I_p \sigma_x$ and the α -loop current operator is $I_{\text{cir},\alpha} = I_+ I_0 + I_- \sigma_z$, where I_0 is the identity operator. I_- is the difference between the α -loop circulating currents, which depend on the ground and excited qubit states. This mechanism enables a σ_z -type interaction (i.e., the longitudinal coupling).

As shown in Refs. [51,52], if there is a mutual inductance M_p between the main loop and the superconducting quantum-interference device (SQUID) of the resonator, one can also couple the σ_x operator with the resonator via

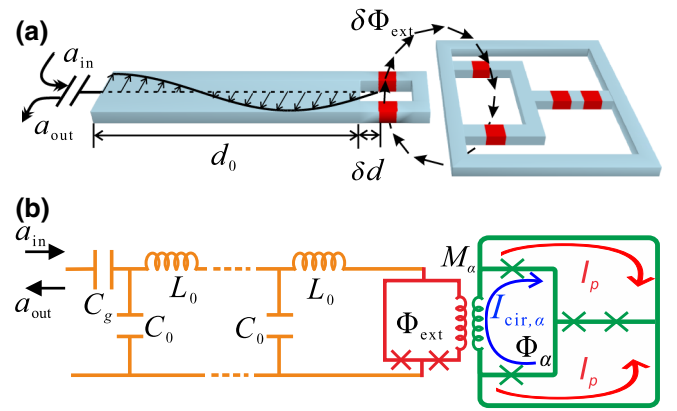


FIG. 1. (a) Schematic and (b) lumped-circuit diagrams of a SQUID-terminated $\lambda/4$ resonator interacting with a gradiometric four-Josephson-junction flux qubit [38] via the mutual inductance M_α . This interaction is due to NPDC as follows: $I_{\text{cir},\alpha}$ (related to the qubit operator σ_z) generates a flux perturbation on the bias flux $\delta\Phi_{\text{ext}}$, which in turn changes the effective length d_0 of the resonator by an amount δd . The result is a dispersive interaction where the photon-number operator $a^\dagger a$ couples to the qubit-state operator σ_z . The resonator capacitance and inductance per unit length are C_0 and L_0 , respectively. The red bars in (a) and the green crosses in (b) represent the Josephson junctions. To dispersively read out the qubit state, one can apply an input field a_{in} via the capacitance C_g . The output field is denoted by a_{out} .

the persistent current I_p . The corresponding coupling is

$$H_p = \chi_x^D \sigma_x a^\dagger a, \quad \chi_x^D = RM_p I_p. \quad (3)$$

A similar type of interaction was discussed in Refs. [52–54], where quantum Zeno effects and qubit-projective measurements were demonstrated with a flux qubit based on three Josephson junctions. H_p does not commute with σ_z and, therefore, cannot be used for QND measurements at the degeneracy point. To read out a given qubit state, one should adiabatically tune the main-loop flux far away from the degeneracy point without damaging the qubit state [36,49]. However, this method suffers from a quick qubit dephasing (away from the degeneracy point) and extra adiabatic operating steps. In our discussions, we focus on the QND measurement based on H_α .

As shown in Fig. 1, we use a resonator terminated by a SQUID [55–62] to detect the quantized current $\hat{I}_{\text{cir},\alpha}$. The resonator is open-ended on its left side, while it is terminated to ground via the SQUID on its right side. The two JJs of the SQUID are symmetric with identical Josephson energy E_{S0} and capacitance C_s , and the effective Josephson energy of the SQUID is tuned by the external flux Φ_{ext} according to $E_S = 2E_{S0} \cos(\pi\Phi_{\text{ext}}/\Phi_0)$, where Φ_0 is the flux quantum. The SQUID has a tunable nonlinear inductance $L_S(\Phi_{\text{ext}}) = \Phi_0^2/[4\pi^2 E_S(\Phi_{\text{ext}})]$ [57–60,63].

Both the SQUID nonlinear inductance $L_S(\Phi_{\text{ext}})$ and the SQUID capacitance C_s are much smaller than the total

capacitance $C_t = d_0 C_0$ and inductance $L_t = d_0 L_0$ of the resonator. On the basis of a distributed-element model and its boundary conditions (see Appendix B), the resonator fundamental mode is of quarter wavelength ($\lambda/4$) and its eigenfrequency depends on the SQUID nonlinear inductance $L_s(\Phi_{\text{ext}})$, and can be tuned via Φ_{ext} according to the following relations:

$$\omega_{r0} = \omega_0 \left[1 - \frac{L_s(\Phi_{\text{ext}}^0)}{L_t} \right], \quad (4a)$$

$$R = \left. \frac{\partial \omega_r}{\partial \Phi_{\text{ext}}} \right|_{\Phi_{\text{ext}}^0} = -\frac{\pi \omega_0 L_s(\Phi_{\text{ext}}^0)}{\Phi_0 L_t} \tan \left(\frac{\pi \Phi_{\text{ext}}^0}{\Phi_0} \right), \quad (4b)$$

where we assume that the external flux Φ_{ext} is composed of a prebiased static part Φ_{ext}^0 and a small deviation part $\delta\Phi_{\text{ext}} \ll \Phi_{\text{ext}}^0$. Similarly to the discussions in Ref. [60] and its experimental realization in Ref. [63], this parametric boundary condition changes the resonator effective length d_0 slightly, which is akin to a moving mirror for modulating the effective wavelength in the optomechanical system. R is the sensitivity of the frequency ω_r tuned by the external flux Φ_{ext} , and ω_{r0} is the renormalized mode frequency. As discussed in Refs. [55,61,64], the attached SQUID introduces a Kerr nonlinearity (K_D) to the whole circuit, which is proportional to $[L_s(\Phi_{\text{ext}})/L_t]^3$ and is

given as [63]

$$K_D \approx -\frac{\pi e^2 \omega_{r0}^2 L_t}{8} \left[\frac{\pi L_s(\Phi_{\text{ext}})}{2L_t} \right]^3. \quad (5)$$

Figure 2 shows the flux sensitivity R and the Kerr nonlinearity K_D versus the applied flux Φ_{ext} . When biasing Φ_{ext} from zero to approximately $\Phi_0/2$, one finds that both $|R|$ and K_D increase rapidly from zero. This indicates that the SQUID is a highly nonlinear element and can be used to enhance nonlinear couplings. In our proposal, the static flux bias Φ_{ext}^0 is prebiased by an external field, while the flux deviation $\delta\Phi_{\text{ext}}$ is generated by the circulating current $I_{\text{cir},\alpha}$ of the flux qubit. As shown in Appendix D, one can use the SQUID-terminated resonator to detect the qubit state, and the Hamiltonian for this system becomes

$$H_\alpha = \omega'_r a^\dagger a + \frac{\omega_q}{2} \sigma_z + \chi_z^D \sigma_z a^\dagger a + K_D (a^\dagger a^\dagger a a), \quad (6)$$

where $\chi_z^D = RM_\alpha I_-$ is the NPDC strength. The identity-matrix term in $I_{\text{cir},\alpha}$ only slightly renormalizes the mode frequency as $\omega'_r = \omega_{r0} + RM_\alpha I_+$. H_α commutes with σ_z , indicating that a qubit readout via H_α is not deteriorated by intracavity photons. Apparently, compared with H_d [Eq. (1)] based on the Rabi model, H_α has no relation to the dipole-field coupling but results from the circulating current $I_{\text{cir},\alpha}$ of the flux qubit affecting the effective length of the resonator. The Purcell-decay and

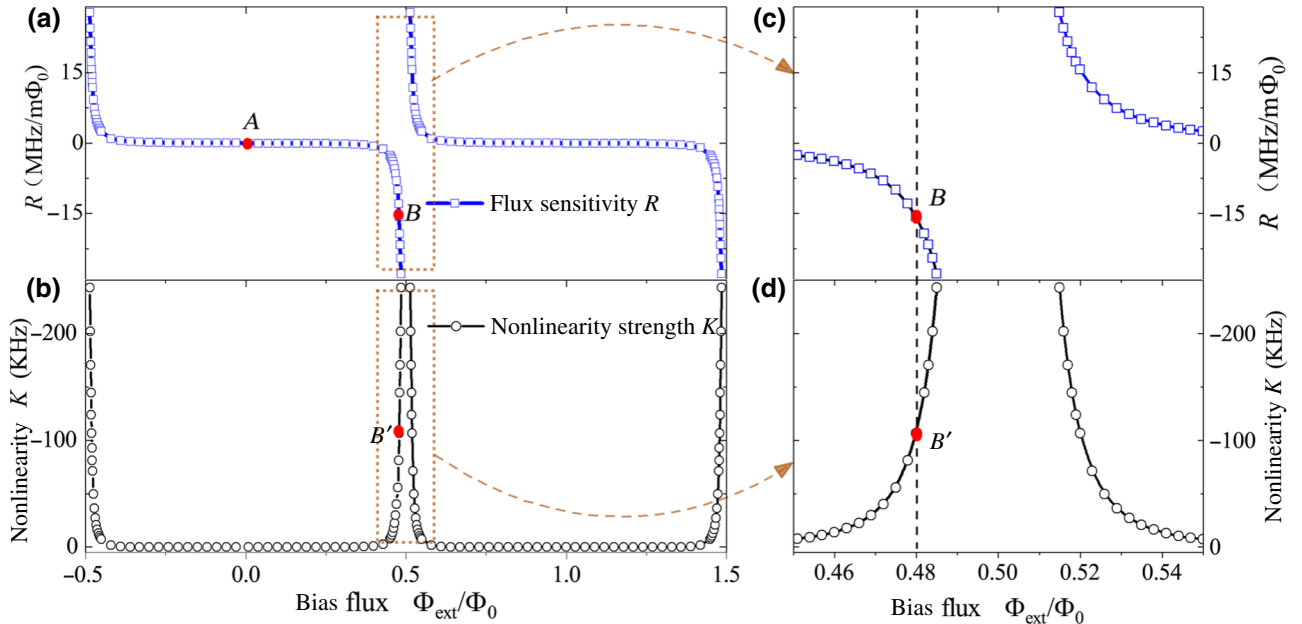


FIG. 2. (a) Resonator flux sensitivity R and (b) its Kerr nonlinearity K versus the SQUID flux bias Φ_{ext} . Parameters are adopted from the experiments reported in Refs. [62,63]: $\omega_0/2\pi = 6$ GHz, $E_s/2\pi = 2.5$ THz, and $L_r = 10$ nH. Point A (B) corresponds to the qubit-resonator decoupling (coupling) regime. (c),(d) show, respectively, the local enlarged plots of (a),(b), respectively, for $\Phi_{\text{ext}} \in [0.45, 0.55]$.

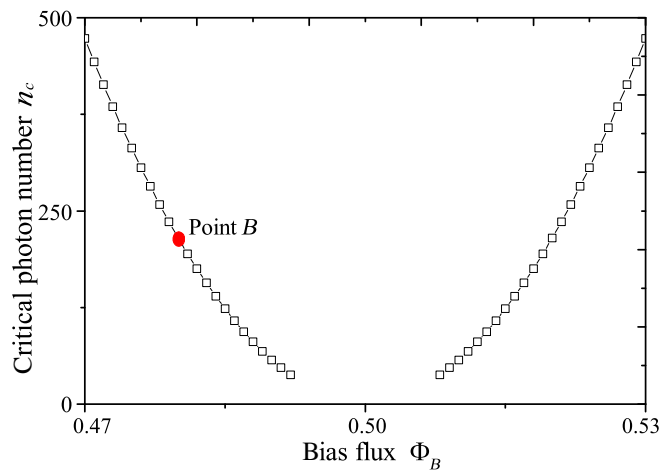


FIG. 3. Critical photon number n_c versus the bias flux Φ_{ext} . The red point corresponds to point B in Fig. 2. The parameters assumed here are the same as those for Fig. 2.

critical-measuring-photon-number limitation are effectively eliminated. Moreover, we can ignore higher-energy-level transitions because the described NPDC is induced without dipole-field interactions. As a result, both quantum-information-processing fidelity and qubit-readout fidelity can be improved compared with other methods affected by higher-energy-level transitions. In fact, this is the core mechanism and advantage of the QND readout based on H_α in our proposal.

However, in dispersive-readout experiments, because the readout resonator is a nonlinear circuit element, one cannot inject plenty of photons without any limitation. As discussed in Appendix B, we assume that the attached SQUID is approximately a harmonic element, which corresponds to adopting the quadratic approximation for the SQUID potential. We expand its cosine potential as a quartic function. This approximation leads to the critical intracavity photon number

$$n_c = |\alpha_c|^2, \quad \alpha_c = \frac{\Phi_0 \sqrt{2\omega_r C_l}}{4\pi \cos\left(\frac{\pi\omega_r}{2\omega_0}\right)}, \quad (7)$$

above which the dispersive-readout process cannot be realized effectively. In Fig. 3, we plot n_c versus the bias flux Φ_{ext} . The red point corresponds to point B in Fig. 2. We find that the critical number decreases quickly when $\Phi_{\text{ext}} \rightarrow 0.5$. This sets an upper bound when this circuit layout is used for the flux qubit readout, as discussed in the next section.

Another advantage of this NPDC-based layout is that the dispersive coupling χ_z^I can be switched on or off by tuning Φ_{ext} . When implementing a gate operation on the qubit, one can bias the flux at $\Phi_{\text{ext}} = N\Phi_0$ [where N is an integer, see point A in Fig. 2(a), the flux sensitivity R is

zero, so $\chi_z^D = 0$]. The readout resonator decouples from the qubit and does not disturb quantum-information processing. Once a qubit readout is required, one can reset Φ_{ext} around $N\Phi_0/2$ (point B) to re-establish the coupling, which is fast and takes only several nanoseconds according to Ref. [56].

The longitudinal degree of freedom of a flux qubit for quantum-information processing was analyzed in, for example, Refs. [65–68], including gate operations without Purcell limitations. Another related work [17] achieved fast qubit readout via parametric modulation of the longitudinal coupling. Compared with our methods, parametric modulation shifts the qubit frequency in a time-dependent manner with a large amplitude. Moreover, higher-order effects, which are induced by the modulation process, might also destroy the readout fidelity of the system in Ref. [17]. Two other recent papers [69,70] on dispersive coupling were based on a Jaynes-Cummings-type Hamiltonian. Therefore, the Purcell effects (although they could be suppressed by the Purcell filters) still exist and limit the qubit-readout fidelity of the systems in Refs. [69,70]. Compared with these studies, our methods can avoid the Purcell effects effectively.

For the qubit, the circulating-current difference I_- in the α loop is about 1 order lower than I_p . At point B in Figs. 2(c) and 2(d), the flux sensitivity $|R|/2\pi \simeq 16$ MHz/m Φ_0 (point B) with nonlinearity $K_D/2\pi \simeq 110$ kHz (point B'). To avoid this Kerr nonlinear effect, one must ensure that $\chi_z^D \gg K_D$.

The mutual inductance between two circuit elements can be (i) geometric, (ii) kinetic, and (iii) nonlinear Josephson inductance. Usually the geometric inductance is very small. However, the kinetic inductance can be very large by sharing a nanowire between two circuit elements [71–73]. The kinetic inductance increases when the cross-section area of a nanowire made from aluminum film is decreased. To achieve stronger χ_z^D , one can use the kinetic mutual inductance M_α by sharing a branch of the α loop with the resonator SQUID [39,74–77]. As discussed in an experimental paper [49], the kinetic inductance per unit length L_k can be 5 pH/ μm for cross-section area $S = 100 \times 90$ nm². Therefore, the value of 15 pH can be easily achieved and the NPDC strength $\chi_z^D/2\pi \simeq 7$ MHz, which is of the same order as the IDC strength reported in experiments [30,78] and strong enough for a qubit QND readout.

Another method is to use a Josephson junction as a mutual inductance. In Ref. [79], the Josephson inductance was reported to be as large as 40 pH. In an experimental realization, one can use a much-larger inductance to achieve even-stronger NPDC than that estimated in this paper. The coupling strength χ_z^D can still be enhanced by reducing the wire cross-section area of the kinetic inductance or by inserting a nonlinear JJ inductance at the connecting position [79,80].

III. NONPERTURBATIVE DISPERSIVE QUBIT READOUT

On the basis of the layout in Fig. 1, one can realize an ideal QND readout of the flux qubit via the coupling Hamiltonian H_α without it being disturbed by the Purcell effects. To compare the IDC and NPDC readouts of the qubit, below we assume

$$\chi_z^I = \chi_z^D = \chi_z, \quad K_D = K_I = K. \quad (8)$$

If an incident field a_{in} is applied in the left port of the resonator at resonator frequency ω'_r , the quantum nonlinear Langevin equation for the resonator operator reads

$$\frac{da(t)}{dt} = -i\chi_z\sigma_z a(t) - 2iK\langle N(t) \rangle a(t) - \frac{1}{2}\kappa a(t) - \sqrt{\kappa}a_{\text{in}}(t). \quad (9)$$

For the IDC readout, $\langle N(t) \rangle = \langle n(t) \rangle \sigma_z$ is due to the qubit-dependent Kerr nonlinearity, where $\langle n(t) \rangle = \langle a^\dagger(t)a(t) \rangle$ is the average intracavity photon number. For the NPDC-based readout mechanism, $\langle N(t) \rangle = \langle n(t) \rangle$ results from the standard Kerr term. This input field $a_{\text{in}}(t) = \alpha_{\text{in}} + d_{\text{in}}(t)$ is characterized by its mean value (a coherent drive) $\alpha_{\text{in}} = -\epsilon e^{i\theta_d}/\sqrt{\kappa}$ and fluctuation $d_{\text{in}}(t)$. Because of the dispersive coupling, the qubit state is encoded in the output quadrature $Y(\phi_h) = a_{\text{out}}^\dagger e^{i\phi_h} + a_{\text{out}} e^{-i\phi_h}$. The measurement corresponds to a homodyne detection of $Y(\phi_h)$ with integration time τ ; that is,

$$M(\tau) = \sqrt{\kappa} \int_0^\tau Y(\phi_h) dt. \quad (10)$$

We first consider an ideal readout with $K = 0$. By formally integrating Eq. (9) and using the input-output relation $a_{\text{out}} = \sqrt{\kappa}a + a_{\text{in}}$, we obtain the separation signal $M_s = \langle M_s \rangle_{|e\rangle} - M_{s,|g\rangle}$ (with $\langle \sigma_z \rangle = \pm 1$) as

$$M_s(\tau) = 4\epsilon \sin 2\theta_q \sin(\theta_d - \phi_h) \times \left\{ \tau - \frac{4 \cos^2 \theta_q}{\kappa} \left[1 - \frac{\sin(\chi_z \tau + 2\theta_q)}{\sin 2\theta_q} e^{-(1/2)\kappa\tau} \right] \right\}, \quad (11)$$

where $\theta_q = \arctan(2\chi_z/\kappa)$ is the rotation angle of the output field. We integrate the Langevin equation in Eq. (E2) to obtain Eq. (E4), which shows the coherent amplitudes α of the intracavity field. In our derivation, we approximately use the classical part of the intracavity field operator to describe the photon number; that is, $\langle n(t) \rangle = |\alpha(t)|^2$. As

derived in Appendix E, $\langle n(t) \rangle$ is given by

$$\langle n(t) \rangle = \left(\frac{2\epsilon}{\kappa} \right)^2 \cos^2 \theta_q \left[1 + \exp(-\kappa t) - 2 \cos(\chi_z \langle \sigma_z \rangle t) \exp\left(-\frac{1}{2}\kappa t\right) \right]. \quad (12)$$

In the steady state ($\kappa t \gg 1$), the intracavity photon number $n \simeq (2\epsilon/\kappa)^2 \cos^2 \theta_q$. The fluctuation $d_{\text{out}}(t)$ introduces noise into the measurement signal. For the vacuum input, the noise reads [28]

$$M_N^2(\tau) = [\langle M_N^2(\tau) \rangle_{|e\rangle} + \langle M_N^2(\tau) \rangle_{|g\rangle}] = 2\kappa\tau. \quad (13)$$

In the long-time limit $\kappa\tau \gg 1$, the signal-to-noise-ratio $\mathcal{R} = M_s(\tau)/M_N(\tau)$ is optimized by setting $\theta_d - \phi_h = \pi/2$ and $\theta_q = \pi/4$ (i.e., $\chi_z = \kappa/2$). The measurement fidelity is defined as

$$F_m = \frac{1 + \text{erf}(\mathcal{R}/2)}{2}, \quad (14)$$

where $\text{erf} x$ is the error function.

As discussed in Appendix E, the effects of the nonlinearities in the IDC and NPDC readouts are different: the Kerr nonlinearity in the IDC readout is qubit dependent, and symmetrically reduces the effective cavity pull [25], which causes a poor signal separation if $\langle a^\dagger(t)a(t) \rangle$ is large. For the NPDC readout, K leads to asymmetric rotation angles of the cavity field in phase space. However, the signal-separation distance is still great, even for large $\langle a^\dagger(t)a(t) \rangle$. Moreover, for the IDC-based readout mechanism, because $[H_x, \sigma_z] \neq 0$, H_d is not an ideal QND readout Hamiltonian. There is a qubit Purcell-decay channel Γ_p via the readout resonator, which is proportional to the photon escape rate κ . Assuming the qubit relaxation is limited by the Purcell decay, the readout signal-to-noise-ratio can be numerically derived by replacing σ_z by

$$\langle \sigma_z \rangle(t) = [1 + \langle \sigma_z \rangle(0)] \exp(-\Gamma_p t) - 1 \quad (15)$$

in Eq. (9). It is hard to obtain analytical results for Eq. (9) by including both K and Γ_p . Thus, below we present only numerical results [81,82]. We first plot the signal-to-noise-ratio versus time in Fig. 4(a). In the IDC readout, due to the Purcell decay, the signal-to-noise-ratio decreases after reaching a maximum. In our simulations, the separation signal M_s indeed saturates at a constant level when the measurement time increases. However, in Fig. 4(a), we plot the signal-to-noise-ratio, which is defined as $\mathcal{R} = M_s/\sqrt{2\kappa\tau}$. When the measurement time τ increases, the signal separation M_s finally reaches its steady value, while a homodyne detector continuously collects the input noise. Therefore, in our discussions, the signal-to-noise-ratio decreases with time as shown in Fig. 4(a). Our definition is

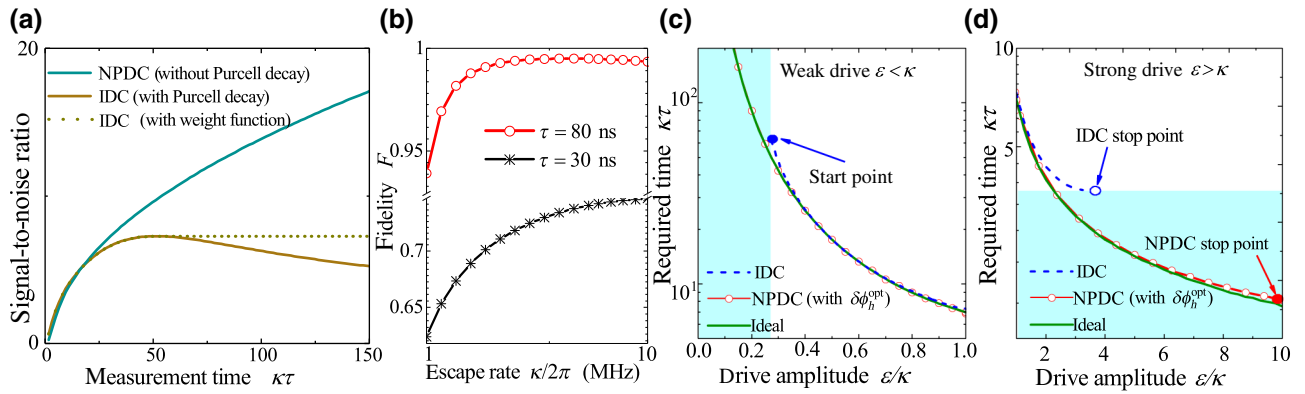


FIG. 4. (a) Signal-to-noise ratio for the NPDC-based and IDC-based readout mechanisms versus the integrated measurement time $\kappa\tau$. (b) Measurement fidelity F_s versus photon escape rate κ at $\tau = 30$ ns and $\tau = 80$ ns. In (a),(b) we set $\epsilon = \chi_z$. (c),(d) The measurement time $\kappa\tau$ required to reach a fidelity of 99.99% versus the drive amplitude ϵ for (c) weak ($\epsilon/\kappa < 1$) and (d) strong ($\epsilon/\kappa \geq 1$) drives. In the IDC readout, the solid (empty) circle marks the start (stop) point, indicating the lower (upper) bound of ϵ . In the NPDC readout, we use the optimal shifted homodyne angle $\delta\phi_h^{\text{opt}}$ for different drive strengths, as discussed in Appendix E. The solid red point is the NPDC stop point due to the nonlinear effects. We set the parameters as $\lambda = 0.1$, $K/2\pi = 100$ kHz, $\chi_z/2\pi = 8$ MHz, and $\kappa/2\pi = 16$ MHz. The cyan areas are the regimes that cannot be reached in the IDC-based readout mechanism due to the Purcell effects.

different from that in the experimental studies [16,83,84]. The weight function $W(t)$ determines how much of the signal power is integrated at time t . This function $W(t)$ can, in principle, be chosen as a square (boxcar) function or can be optimized on the basis of certain experimental implementations [16]. In Fig. 4(a), we use a simple square function, which leads to a constant value of the signal-to-noise-ratio after it has reached its highest point.

For the NPDC readout, the escaping photon does not lead to the decay of the qubit states, and the signal-to-noise-ratio is proportional to $\sqrt{2\kappa\tau}$ in the long-time limit $\kappa\tau \gg 1$ [17,28]. One may try to suppress Γ_p by reducing κ . However, to achieve a fast qubit readout, κ should be large enough to allow readout photons to escape quickly. The relation can be clearly found in Fig. 4(b): for a certain integrated time τ , the readout fidelity increases with κ . Therefore, to reduce the Purcell decay, one should decrease the measurement speed with a relatively low κ in the IDC readout. However, this trade-off relation does not exist in the NPDC readout: it is without dipole-field coupling, and the qubit QND readout is not disturbed by the Purcell decay. One can use a large κ to speed up the readout.

As shown in Fig. 5 (with the same measurement time $\kappa\tau = 3$), one can find that the Wigner functions for the IDC-based and NPDC-based readout mechanisms are not perfectly symmetric Gaussian functions. This is due to the Kerr nonlinearity, which modifies the coherent state of the resonator field. Consequently, the collected noise in the homodyne measurement for a given quadrature direction in phase space can be different from the ideal result given in Eq. (13) assuming a classical resonator field. Nevertheless, we use the Heisenberg-Langevin equation and treat the resonator field as classical in Fig. 4. Precise numerical calculations of the evolution of our system, including

the quantized resonator field with many injected photons, require one to assume a Hilbert-space dimension on the order of hundreds and thus require time-consuming numerical calculations. However, for the parameters considered in this work, treating the resonator field to be coherent leads to only a very small difference compared with the fully quantum treatment of the entire system.

To verify this classical approximation of the resonator field, we plot Fig. 6 by applying the quantum treatment of the resonator field for the parameters at the IDC stop point in Fig. 4(d). Figure 6 shows the effect of the quantum noise $M_N(\tau)$ changing with the measurement time for the ideal,

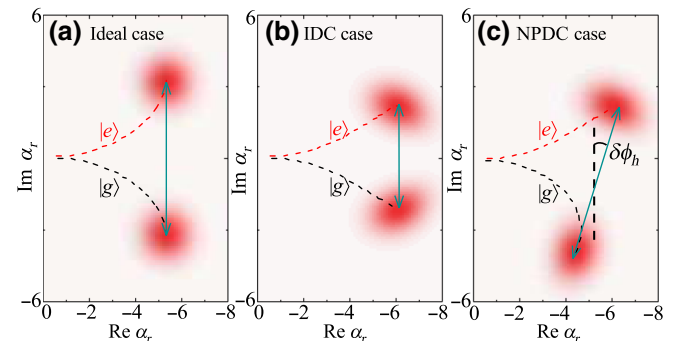


FIG. 5. The Wigner distributions of the intracavity field for the (a) ideal, (b) IDC, and (c) NPDC readouts for the same measurement time $\kappa\tau = 3$. The red (black) curves are the time-dependent evolution trajectories in phase space, and the upper (lower) signals correspond to the qubit being in its excited (ground) state. The arrows represent signal-separation distances and directions. The parameters use here are the same as those in Fig. 4(d), and the drive strength is assumed to be the same as for the stop point. For the NPDC readout in (a), the signal-separation direction is rotated by an angle $\delta\phi_h$.

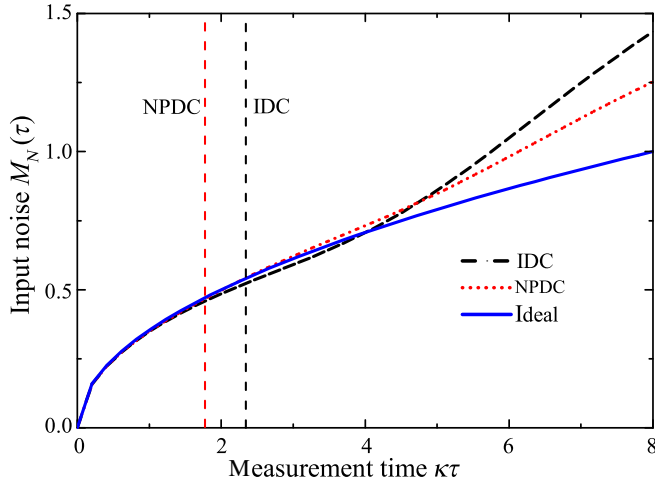


FIG. 6. The measurement noise $M_N(\tau)$ for the ideal, IDC, and NPDC readouts obtained by quantum simulations. The dashed lines correspond to the required measurement time for the IDC and NPDC proposals. The parameters assumed here are the same as those for the stop point of the IDC readout shown in Fig. 4(d).

NPDC, and IDC readouts. The vertical lines correspond to the required time for the IDC and NPDC readouts in Fig. 4(d), respectively, where the noise shift, which is induced by the Kerr effect, is negligible compared with the ideal-readout case and one can use our analytical results given in Eq. (13) to calculate the signal-to-noise-ratio. If one insists on achieving a higher fidelity, the required time becomes longer and thus one should calculate the input quantum noise changing with the measurement time for different methods in the fully quantum treatment of the resonator field. Moreover, by comparing the IDC and NPDC results in the long-measurement-time limit ($\kappa\tau \gg 1$), we find that the noise for the NPDC readout increases more slowly compared than the noise for the IDC readout. This is another advantage of our proposal.

In Figs. 4(c) and 4(d), we plot the time $\kappa\tau$ required to reach a fidelity of 99.99% as a function of the drive strength ϵ . Figure 4(c) corresponds to the weak-drive limit ($\epsilon < \kappa$). Because of the qubit Purcell decay, there is a lower limit of ϵ_{\min} (start point) for the drive amplitude in the IDC readout. If $\epsilon < \epsilon_{\min}$ (cyan area), the measurement can never reach the desired fidelity even if it takes an infinitely long time. However, for the NPDC readout (dotted red curve) based on our proposal, the ideal fidelity can be reached in principle for $\epsilon < \epsilon_{\min}$.

For the NPDC-based readout mechanism, we cannot increase the photon number due to some limitations of Eq. (7). In Fig. 4(d), we mark the corresponding stop point (due to n_c) for the NPDC readout (solid red point), which is around $\epsilon/\kappa \simeq 10$ and far from the stop point of the IDC readout. The critical photon number n_c decreases when the flux bias Φ_{ext} is close to $\Phi_0/2$. As shown in Fig. 2, there is a trade-off relation between the flux sensitivity R (i.e.,

the NPDC coupling strength) and n_c , which might be one of the obstacles for achieving much-shorter readout times. In future studies, to reach the minimum readout time, one could optimize the parameters of the whole readout circuits.

In the strong-drive limit, $\epsilon > \kappa$ [Fig. 4(d)], for both readout mechanisms, the required time $\kappa\tau$ is significantly reduced. Unfortunately, the IDC-based readout mechanism encounters another two Purcell limitations: First, the effective cavity pull is significantly reduced as

$$|\xi_I| = \left| \chi_z \left(1 - \frac{\langle n(t) \rangle}{2n_c} \right) \right|, \quad (16)$$

which leads to a reduction of the signal separation. By comparing Figs. 5(a) and 5(b), it can be found that for the IDC readout, the signal-separation distance (olive arrows) in phase space is much smaller than that for the ideal readout. Consequently, the required time becomes much longer than that for the ideal readout. Second, to avoid photon-induced qubit-error transitions, the intracavity photon number should be much smaller than the critical photon number $n_c = 1/(4\lambda^2)$. This sets another upper-bound limitation $\epsilon_{\max} = \kappa/(2\sqrt{2}\lambda)$ for the drive strength [10]. The measurement time τ cannot be shortened below the stop point.

For large $\langle n(t) \rangle$, the Kerr nonlinearity in the NPDC-based readout mechanism also induces apparent effects. However, as shown in Fig. 5, its main effect is to change the signal separation direction with a small angle $\delta\phi_h$ [61], while the signal separation distance is still large compared with that for the IDC readout. Moreover, intracavity photons do not cause qubit-state error flips and, therefore, in principle, there is no such stop point due to the Purcell effects. To minimize the Kerr effects, we can slightly shift the homodyne angle ϕ_h by an optimized small angle $\delta\phi_h^{\text{opt}}$. The detailed method for how to shift the measurement angle can be found in Appendix E. As seen in Fig. 4(d), the required time can be quite close to that for the ideal readout. Therefore, by injecting many photons, one can decrease the measurement time far below the Purcell-effect regime.

IV. DISCUSSION

A. Multiqubit readout via a single resonator

It is also possible to use an array of SQUIDs to terminate the measurement resonator (see Ref. [56]). As discussed in Appendix B, the effective nonlinear inductance of each SQUID can be tuned independently via the flux $\Phi_{\text{ext},j}$ produced by an individual flux-bias line. For the j th SQUID interacting with the j th flux qubit ($\sigma_{z,j}$) via its circulating

current $I_{\text{cir},\alpha j}$, the interaction Hamiltonian is

$$H_{\alpha,\Sigma} = \sum_j \chi_{z,i} \sigma_{z,j} a^\dagger a, \quad \chi_{z,i} = R(\Phi_{\text{ext},j}) I_{\text{cir},\alpha j} M_j, \quad (17)$$

with M_j being the mutual inductance. To read out the m th qubit without the readout being disturbed by other qubit-resonator couplings, one can tune $R(\Phi_{\text{ext},j})$ to zero with $\Phi_{\text{ext},j} = 0$ for $j \neq m$, while keeping $R(\Phi_{\text{ext},m})$ around point B (see Fig. 2). In this case, the resonator is used as a shared readout resonator for each individual qubit. Moreover, we could realize a joint readout of multiqubit states [78]. For the example of two qubits, we set $\chi_{z,1}/2 = \chi_{z,2} = \chi_0$. The two-qubit basis $\{|e, e\rangle, |e, g\rangle, |g, e\rangle, |g, g\rangle\}$ corresponds to four different rotation angles (in phase space) $\theta_{qN} = \arctan(N\chi_0/\kappa)$, with $N = \pm 1, \pm 3$ for the output field, which represents four separated pointer states. This multi-SQUID layout enables scalability for an ideal qubit joint QND readout.

If we assume similar values of the flux sensitivity $R(\Phi_{\text{ext},j})$ of all the SQUIDs (labeled by the index j), the phase drops across each SQUID are also similar [61]. Because of this property, the Kerr nonlinearity K'_D increases linearly with the SQUID number n ; that is, $K'_D = nK_D$. In all our discussions, the Kerr nonlinearity always decreases the readout fidelity. Therefore, this scalable proposal works well when we are considering only a few SQUIDs and a weak drive field. Beyond these regimes, we should find better proposals for such a qubit QND readout.

B. Dynamical range of the SQUID-terminated resonator

Finally, we discuss the dynamical range of the measurement SQUID-terminated resonator. The differential equation (9) for NPDC readout is nonlinear, and the steady-state solution for the intracavity photon number can be solved from a cubic equation. To analyze this problem, we need to define the dimensionless effective detuning as

$$\delta^s = \frac{\chi_z^D}{\kappa} \langle \sigma_z \rangle, \quad \delta^s \in \left[- \left| \frac{\chi_z^D}{\kappa} \right|, \left| \frac{\chi_z^D}{\kappa} \right| \right]. \quad (18)$$

As derived in Ref. [61], the critical detuning $\delta_{\text{crit}}^s = -\sqrt{3}/2$, below which the cubic equation might have three solutions for the intracavity-field intensity. Both the smallest solution and the largest solution are stable for the whole system. However, the intermediate one is unstable, around which the field in the readout resonator might bifurcate. During the dispersive readout, it is better for the system to avoid this highly nonlinear regime.

As shown Fig. 4(b), a rapid photon escape rate κ increases the readout fidelity. In an experimental implementation, if a large κ is adopted, the dimensionless detuning $|\delta^s|$ is a small parameter. For example, in Figs. 4(c)

and 4(d), we adopt $\delta^s \in [-1/2, 1/2]$, which is out of the bistable regime. Therefore, our proposal can effectively avoid bistability problems induced by the Kerr nonlinearity.

V. CONCLUSIONS

We show how to realize an ideal QND readout of a flux qubit via its nonperturbative dispersive coupling with a SQUID-terminated measurement qubit. The coupling can be conveniently switched on and off via an external flux control. Compared with the conventional induced dispersive coupling based on the Rabi model, this mechanism is free of dipole-field interactions and, therefore, it is not deteriorated by the Purcell effects. We can use a strong drive field and a fast photon escape rate. Thus, both measurement fidelity and measurement speed can avoid the Purcell limitations. For a single resonator, which is terminated by a series of SQUIDs, this proposal is scalable and tunable to realize a multiqubit joint QND readout. In future studies, this proposed method might be developed to include a weak continuous measurement to monitor the superconducting flux qubit [85,86]. Moreover, this method can be applied to other weak-signal measurements, such as detecting virtual photons or qubit excited states in the ultrastrong light-matter coupling regime [87,88].

ACKNOWLEDGMENTS

The authors acknowledge fruitful discussions with Xiu Gu, Yu-Xi Liu, Zhi-Rong Lin, and Wei Qin. X.W. thanks Yun-Long Wang for helping to depict the schematic diagrams. X.W. is supported by China Postdoctoral Science Foundation Grant No. 2018M631136 and the National Natural Science Foundation of China under Grant No. 11804270. A.M. and F.N. acknowledge the support of a grant from the John Templeton Foundation. F.N. is supported in part by the: MURI Center for Dynamic Magneto-Optics via the Air Force Office of Scientific Research (AFOSR) (FA9550-14-1-0040), Army Research Office (ARO) (Grant No. W911NF-18-1-0358), Asian Office of Aerospace Research and Development (AOARD) (Grant No. FA2386-18-1-4045), Japan Science and Technology Agency (JST) (via the Q-LEAP program, and the CREST Grant No. JPMJCR1676), Japan Society for the Promotion of Science (JSPS) (JSPS-RFBR Grant No. 17-52-50023, and JSPS-FWO Grant No. VS.059.18N), the RIKEN-AIST Challenge Research Fund, the Foundational Questions Institute (FQXi), and the NTT-PHI Lab.

Note added.—After the e-print of this work had been posted in arXiv [89], the work of Dassonneville *et al.* [90] on the same topic was posted in arXiv. That paper describes a protocol very similar to ours, but for a different type of superconducting qubit, which can be viewed as an experimental realization of the QND measurement

of superconducting qubits via nonperturbative dispersive coupling. Those studies indicate that the concept of a QND readout via the NPDC mechanism is experimentally feasible and should receive much-more attention, both theoretical and experimental, soon.

APPENDIX A: INDUCED DISPERSIVE COUPLING AND PURCELL DECAY

In a typical system based on superconducting quantum circuits, the conventional light-matter dispersive coupling is based on dipole-field interactions. In the large-detuning regime $g_x \ll \Delta_d = \omega_q - \omega_a$ (where ω_q and ω_r are the qubit frequency and resonator frequency, respectively), the system Hamiltonian is approximately described by the Jaynes-Cummings Hamiltonian:

$$H_{R0} = \frac{\omega_q}{2} \sigma_z + \omega_r a^\dagger a + g_x (a \sigma_+ + a^\dagger \sigma_-). \quad (\text{A1})$$

In a qubit dispersive readout, one often injects many photons into the resonator to speed up such measurement. Once the photon number is large, it is necessary to push the dispersive coupling into higher-order nonlinear terms. Here we follow the approaches in Refs. [25,27], and derive a more-exact nonlinear-dispersive-coupling Hamiltonian. We first define the unitary transformation U_D as [27]

$$U_D = \exp \left\{ -\Theta(N_J) (a^\dagger \sigma_- - a \sigma_+) \right\}, \quad (\text{A2})$$

$$\Theta(N_J) = -\frac{\arctan 2\lambda \sqrt{N_J}}{2\sqrt{N_J}},$$

where

$$\lambda = g_x / (\Delta_d), \quad \Delta_d = \omega_q - \omega_r,$$

and

$$N_J = a^\dagger a + |e\rangle\langle e|$$

is a function of the total-excitation-number operator of the system. If we apply the transformation U_D to the Jaynes-Cummings Hamiltonian H_{R0} , the off-diagonal terms can be eliminated, yielding

$$H_{R0} = \frac{\omega_q}{2} \sigma_z + \omega_r a^\dagger a - \frac{\Delta_d}{2} \left(1 - \sqrt{1 + 4\lambda^2 N_J} \right) \sigma_z. \quad (\text{A3})$$

This equation is still the exact diagonalized solution for the system Hamiltonian without any approximation. To obtain the dispersive coupling, we can expand $\sqrt{1 + 4\lambda^2 N_J}$ to

second order in $4\lambda^2 N_J$ to find [27]

$$H_{R0} = \omega'_r a^\dagger a + \frac{\omega_q}{2} \sigma_z + \chi_z^I a^\dagger a \sigma_z + K_I (a^\dagger a^\dagger a a) \sigma_z, \quad (\text{A4})$$

where ω'_r is the shifted resonator frequency,

$$\chi_z^I = g_x^2 (1 - 2\lambda^2) / \Delta_d \simeq g_x^2 / \Delta_d$$

is the IDC strength, and

$$K_I = -g_x^4 / \Delta_d^3$$

is the qubit-dependent Kerr-nonlinearity strength. The validation of this perturbation result requires that Eq. (A4) does not only depend on a small parameter $\lambda \ll 1$ but also that the total excitation number satisfies $\langle N_J \rangle \ll 1/4\lambda^2$, which results in critical photon $n_c = 1/4\lambda^2$ [10]. In a qubit measurement, the intracavity photon number should be much smaller than n_c .

The coupling Hamiltonian between the measurement and the environment is

$$H_\kappa = \int_0^\infty \sqrt{\kappa(\omega)} [b^\dagger(\omega) + b(\omega)] (a + a^\dagger) d\omega, \quad (\text{A5})$$

where $b(\omega)$ is the annihilation operator of the environmental mode ω . Applying the unitary transformation U_D to the field operators $(a + a^\dagger)$, we obtain

$$U_D^\dagger (a + a^\dagger) U_D \simeq (a + a^\dagger) + \lambda (\sigma_- + \sigma_+) + \mathcal{O}(\lambda^2). \quad (\text{A6})$$

One can find that the field operator acquires an extra part related to the qubit operators σ_\pm in the dressed basis. In the interaction picture and applying the rotating-wave approximation to the Hamiltonian H_κ , we obtain

$$H_\kappa = \int_0^\infty d\omega \sqrt{\kappa(\omega)} [b(\omega) a^\dagger e^{-i(\omega - \omega_r)t} + \text{H.c.}] + \lambda \int_0^\infty d\omega \sqrt{\kappa(\omega)} [b(\omega) \sigma_+ e^{-i(\omega - \omega_q)t} + \text{H.c.}], \quad (\text{A7})$$

where the last term describes an additional Purcell-decay channel for the qubit. The cavity is assumed to couple with a thermal environment with zero average boson number. Following the standard steps of deriving the master equation, we find that the last term adds an extra qubit decay with rate $\Gamma_p = \lambda^2 \kappa(\omega_q)$. In this work, we assume that $\kappa(\omega_q)$ is not frequency dependent and equals the photon escape rate κ .

APPENDIX B: SQUID-TERMINATED TRANSMISSION-LINE RESONATOR

1. Tuning the resonator frequency via a SQUID: linear approximation

As shown in Fig. 1, we consider a TLR (along the x axis with length d_0) short-circuited to ground by terminating its right side with a dc SQUID (at the position $x = d_0$) [55,58]. The two Josephson junctions of the SQUID are assumed to be symmetric with identical Josephson energy E_{s0} and capacitance C_s . The effective Josephson energy of the SQUID is tuned with the external flux Φ_{ext} , according to the relation $E_s = 2E_{s0} |\cos(\pi \Phi_{\text{ext}}/\Phi_0)|$ (Φ_0 is the flux quantum). For an asymmetric SQUID with two different Josephson energies E_{s1} and E_{s2} , the effective Josephson energy of the SQUID is given by

$$E'_s = E_\Sigma \sqrt{\cos^2\left(\frac{\pi \Phi_{\text{ext}}}{\Phi_0}\right) + d_0 \sin^2\left(\frac{\pi \Phi_{\text{ext}}}{\Phi_0}\right)}, \quad (\text{B1})$$

where

$$d_0 = \frac{E_{s1} - E_{s2}}{E_{s1} + E_{s2}} \quad (\text{B2})$$

is the junction asymmetric parameter. From Eq. (B1), the asymmetric effects can be ignored under the condition

$$d_0 < \cot\left(\frac{\pi \Phi_{\text{ext}}}{\Phi_0}\right). \quad (\text{B3})$$

In our work, we consider $\Phi_{\text{ext}}/\Phi_0 \in [0.46, 0.48]$, which results in $d_0 < 7\%$. The present fabrication technology can control the junction asymmetric parameter within $d_0 < 2\%$ [28]. Therefore, the condition in Eq. (B3) is within reach of current experiments [9].

The SQUID has a nonlinear inductance

$$L_s(\Phi_{\text{ext}}) = \frac{\Phi_0^2}{(2\pi)^2 E_s(\Phi_{\text{ext}})}, \quad (\text{B4})$$

and its Lagrangian is written as [55,56]

$$\mathcal{L} = \sum_{i=1,2} \left[\frac{\Phi_0^2 C_s}{2(2\pi)^2} \dot{\phi}_i^2 + E_{s0} \cos \phi_i \right]. \quad (\text{B5})$$

Setting $\phi_+ = (\phi_1 + \phi_2)/2$ and $\phi_- = (\phi_1 - \phi_2)/2 = \pi \Phi_{\text{ext}}/\Phi_0$, we rewrite Eq. (B5) as

$$\mathcal{L} = \frac{\Phi_0^2 C_s}{(2\pi)^2} \dot{\phi}_+^2 + E_s \cos \phi_+. \quad (\text{B6})$$

Given that $E_s \gg (2e)^2/2C$, the zero-point fluctuation in the plasma oscillation is of small amplitude with $\phi_{z0} =$

$\sqrt[4]{4e^2/2C_s E_s} \ll 1$, and the SQUID is around its quantum ground state [60]. The SQUID can be seen as a harmonic oscillator with Lagrangian [55]

$$\mathcal{L} \simeq \frac{\Phi_0^2 C_s}{(2\pi)^2} \dot{\phi}_+^2 - \frac{E_s}{2} \phi_+^2. \quad (\text{B7})$$

We denote the transmission-line capacitance and inductance per unit length as C_0 and L_0 , respectively. The dynamics of the field along the transmission-line direction (denoted as the x axis) is described by the Helmholtz wave equation

$$\frac{\partial^2 \psi(x, t)}{\partial t^2} - v^2 \frac{\partial^2 \psi(x, t)}{\partial x^2} = 0, \quad (\text{B8})$$

where $v = 1/\sqrt{L_0 C_0}$ is the wave velocity. At $x = 0$ with a large capacitance C_g , the boundary condition is $\partial_x \psi(0, t) = 0$, which requires that the wave-function solutions of Eq. (B8) for mode k have the form $\psi(x, t) = \psi_0 \sin(kvt) \cos(kx)$. At $x = d_0$, the boundary conditions are [55,57]

$$\begin{aligned} \psi(d_0, t) &= \phi_+(t), \\ 2C_s \ddot{\psi}(d_0, t) + \frac{(2\pi)^2}{\Phi_0^2} E_s \psi(d_0, t) + \frac{\partial_x \psi(d_0, t)}{L_0} &= 0. \end{aligned} \quad (\text{B9})$$

By substituting the wave function into Eq. (B9), one can find that the mode frequency $\omega_r = vk$ of the resonator can be derived from the following transcendental equation [62]:

$$\frac{\pi \omega_r}{2\omega_0} \tan\left(\frac{\pi \omega_r}{2\omega_0}\right) = \frac{(2\pi)^2}{\Phi_0^2} L_t E_s(\Phi_{\text{ext}}) - \frac{2C_s}{C_t} \left(\frac{\pi \omega_r}{2\omega_0}\right)^2, \quad (\text{B10})$$

where $L_t = d_0 L_0$ and $C_t = d_0 C_0$ are the total inductance and total capacitance of the resonator, respectively. The fundamental frequency of the quarter-wavelength resonator $\omega_0 = \pi v/2d_0$. By assuming that the capacitances of the Josephson junctions C_s are much smaller than the total capacitance C_t , we ignore the last term in Eq. (B10). Because the total inductance L_t strongly exceeds that of the SQUID nonlinear inductance $L_s(\Phi_{\text{ext}})$, we find $\omega_r/\omega_0 \simeq 1$ and rewrite Eq. (B10) as

$$\left[\frac{\pi \omega_r}{2\omega_0} \tan\left(\frac{\pi \omega_r}{2\omega_0}\right) \right]^{-1} = \frac{L_s(\Phi_{\text{ext}})}{L_t}. \quad (\text{B11})$$

By expanding the left-hand side of Eq. (B11) with $\pi \omega_r/2\omega_0$ around $\pi/2$ to first order, we obtain

$$\omega_r = \omega_0 \left[1 - \frac{L_s(\Phi_{\text{ext}})}{L_t} \right]. \quad (\text{B12})$$

From this equation, we find that the external flux Φ_{ext} through the SQUID determines its nonlinear inductance,

which eventually shifts the mode frequency ω_r . Similarly to the discussions in Ref. [57], this parametric boundary condition changes the resonator effective length only slightly, which is akin to a moving mirror for modulating the effective wavelength in the optomechanical system. We assume that the external flux is composed of a prebiased static part Φ_{ext}^0 and a small deviation part $\delta\Phi_{\text{ext}} \ll \Phi_{\text{ext}}^0$ and write the mode frequency as

$$\omega_r = \omega_{r0} + \frac{\partial\omega_r}{\partial\Phi_{\text{ext}}}\bigg|_{\Phi_{\text{ext}}^0} \delta\Phi_{\text{ext}}, \quad (\text{B13})$$

where the shifted mode frequency ω_{r0} and its flux sensitivity R are expressed in Eq. (4). In our discussions we assume that the dc-SQUID loop inductance can be ignored compared with L_s , which can be easily satisfied in experiments [63]. Therefore, the frequency-jump effects of the mode frequency due to its hysteretic flux response can also be ignored [62].

2. Resonator self-Kerr-nonlinearity

Because the SQUID is a nonlinear element, attaching it at the end of the resonator makes the entire system nonlinear. Here we wish to estimate the amount of such nonlinearity. In Eq. (B7), we approximately view the SQUID as a linear circuit element by ignoring the higher-order terms. To obtain the nonlinear terms of this system, we expand the SQUID cosine potential to include nonquadratic corrections. Because $\phi_+ \ll 1$, it is enough to consider its fourth-order terms in the Lagrangian

$$\mathcal{L} = \frac{\Phi^2 C_s}{(2\pi)^2} \dot{\phi}_+^2 - \frac{E_s}{2} \phi_+^2 + \frac{E_s}{24} \phi_+^4 + \dots \quad (\text{B14})$$

The boundary condition in Eq. (B9) now contains the cubic term,

$$2C_s \ddot{\psi}(d_0, t) + \frac{\partial_x \psi(d_0, t)}{L_0} + \frac{(2\pi)^2}{\Phi_0^2} E_s(\Phi_{\text{ext}}) \left[\psi(d_0, t) - \frac{1}{6} \psi^3(d_0, t) \right] = 0. \quad (\text{B15})$$

The cubic term not only relates the boundary equation with both first-harmonic and third-harmonic modes but also produces a shift of the resonant frequency, which depends on the photon number of the resonator mode. Comparing Eq. (B15) with Eq. (B9), we can roughly view the Josephson energy $E_1(\Phi_{\text{ext}})$ to be slightly modified as

$$E_1(\Phi_{\text{ext}}) \rightarrow E_1(\Phi_{\text{ext}}) \left[1 - \frac{1}{6} \psi^2(d_0, t) \right], \quad (\text{B16})$$

which indicates that the nonlinear inductance $L_{s1}(\Phi_{\text{ext}})$ now depends on the intracavity field intensity $\psi^2(d_0, t)$.

Using Eq. (B12), and similarly to the deviation in Ref. [61], we can write the quantized Hamiltonian of the fundamental mode with the self-Kerr-nonlinearity approximately as

$$H = \omega_{r0} a^\dagger a + K_D a^\dagger a^\dagger a a, \quad (\text{B17})$$

with the Kerr-nonlinearity strength

$$K_D = -\frac{\cos^4\left(\frac{\pi\omega_r}{2\omega_0}\right)}{4L_s(\Phi_{\text{ext}})} \left(\frac{2\pi\phi_{\text{ZPF}}^2}{\Phi_0}\right)^2 \approx -\frac{\pi e^2 \omega_{r0}^2 L_t}{8} \left[\frac{\pi L_s(\Phi_{\text{ext}})}{2L_t}\right]^3, \quad (\text{B18})$$

where the quantized form of the field amplitude is

$$\psi_1(t) = \phi_{\text{ZPF}} \left[a \exp(-i\omega_{r0}t) + a^\dagger \exp(i\omega_{r0}t) \right],$$

with

$$\phi_{\text{ZPF}} = \frac{2\pi}{\Phi_0} \sqrt{\frac{1}{2\omega_{r0}C_t}}$$

being the zero-point fluctuation of the flux field [55]. The self-Kerr-nonlinearity is due to our attaching the SQUID at the end of the resonator. In our discussion, the condition $L_s(\Phi_{\text{ext}})/L_t \ll 1$ is always valid, and the Kerr strength K_D is proportional to the cubic order of the small parameter $L_s(\Phi_{\text{ext}})/L_t$, which is much weaker than the first-order effects [Eq. (B12)]. In the following discussions, we consider these Kerr-nonlinearity effects on the qubit-readout process.

We also need to check the validity of the quartic expansion approximation in Eq. (B14), which requires $\phi_+ < 1$. Considering the boundary condition in Eq. (B9), one finds that the amplitude of the intracavity field at position d_0 satisfies

$$\phi_+ = \psi(d_0, t) = 2\phi_{\text{ZPF}} \alpha_c \cos kd_0 < 1, \quad (\text{B19})$$

where $\alpha_c = \langle a \rangle$. Using the relation $kd_0 = \pi\omega_r/2\omega_0$ and according to the transcendental equation (B11), one finds the critical amplitudes given in Eq. (7). In our discussions, we assume that ω_r is approximately ω_0 , which results in a large critical photon number $n_c = |\alpha_c|^2$.

3. Resonator pure dephasing due to tunable boundary conditions

Differently from a frequency-fixed resonator, the mode frequency of the SQUID-terminated resonator depends on external parameters. The bias noise of these control parameters leads to dephasing processes of the resonator, which is similar to the qubit case [91–93]. In our proposal, the mode frequency is tuned via the flux bias through the

SQUID and the Josephson energy. The bias flux noise might come from the external control lines, and the most important part is the $1/f$ noise. Moreover, the noise in the critical current I_c of each junction may result in fluctuations of the Josephson energy via the relation $E_{s0} = I_c \Phi_0 / 2\pi$ [94]. Consequently, the resonator Hamiltonian can be formally written as

$$H_r = \omega_{r0} a^\dagger a + \left[\frac{\partial \omega_r}{\partial \Phi_{\text{ext}}} \delta \Phi_N(t) + \frac{\partial \omega_r}{\partial I_c} \delta I_N(t) \right] a^\dagger a, \quad (\text{B20})$$

where $\delta \Phi_N(t)$ and $\delta I_N(t)$ are the flux and critical-current fluctuations around the static biases. For convenience we set

$$f_1(t) = \frac{\partial \omega_r}{\partial \Phi_{\text{ext}}} \delta \Phi_N(t), \quad f_2(t) = \frac{\partial \omega_r}{\partial I_c} \delta I_N(t).$$

In the shifted frame of frequency ω_{r0} , decoherence processes can be defined via the time-dependent off-diagonal operator

$$a(t) = \exp(-i\omega_{r0}t) \left\langle \exp \left[-i \int_0^t dt' \sum_{i=1,2} f_i(t') \right] \right\rangle. \quad (\text{B21})$$

The phase of the off-diagonal terms of $\langle a(t) \rangle$ acquires a random term $-i \int_0^t dt' \sum_{i=1,2} f_i(t')$. The time average of the fluctuation correlation function is defined by its noise power, which is expressed as

$$\langle f_i(t) f_i(0) \rangle = \frac{1}{2\pi} \int_{-\infty}^{\infty} d\omega S_i(\omega) \exp i\omega t. \quad (\text{B22})$$

Usually, the integrated noise is given by a Gaussian distribution, and there is no correlation between these two different noise sources. Similarly to the discussions in Refs. [91–93], we obtain the following relation:

$$\begin{aligned} & \left\langle \exp \left[-i \int_0^t dt' \sum_{i=1,2} f_i(t') \right] \right\rangle \\ &= \exp \left[-\frac{1}{2} \sum_{i=1,2} \left\langle \int_0^t dt' f_i(t') \int_0^t dt'' f_i(t'') \right\rangle \right] \\ &= \exp \left[-\frac{1}{2} \int_{-\infty}^{\infty} \frac{d\omega}{2\pi} W(\omega) \sum_{i=1,2} S_i(\omega) \right], \quad (\text{B23}) \end{aligned}$$

where $W(\omega)$ is the spectral weight function (see, e.g., Ref. [91]) given by

$$W(\omega) = \frac{\sin^2(\omega t/2)}{(\omega/2)^2}. \quad (\text{B24})$$

The noise correlation function $S_i(\omega)$ determines the decoherence behavior of the off-diagonal matrix elements.

Given that the correlation time of the noise is extremely short, $S_i(\omega)$ is almost flat in the frequency domain, and the corresponding line shape is Lorentzian with homogeneous broadening [94]. However, for the $1/f$ noise, its correlation function is approximately described as $S_i(\omega) \propto 2\pi A_i^2 / |\omega|$ with a singularity around $\omega = 0$ [91], where A_i is the noise amplitude. For simplification, we assume that the $1/f$ frequency ranges of both flux noise and critical-current noise are limited by the same infrared (ω_{IR}) and ultraviolet (ω_{UV}) cutoff. In this case, we solve the decoherence rate by substituting $S_i(\omega)$ into Eq. (B23) to obtain [92]

$$a(t) \simeq \exp \left\{ -i\omega_{r0}t - \frac{1}{2} \left[\left(A_1 \frac{\partial \omega_r}{\partial \Phi_{\text{ext}}} t \right)^2 + A_2 \left(\frac{\partial \omega_r}{\partial I_c} t \right)^2 \right] |\ln \omega_{\text{IR}} t| \right\}. \quad (\text{B25})$$

We can roughly treat $\ln \omega_{\text{IR}} t$ as a constant, and find that $\langle a(t) \rangle$ decays with time as t^2 . From Eq. (B25), the estimated dephasing rates $\Gamma_{f,\Phi}$ and $\Gamma_{f,I}$ induced by the $1/f$ flux-noise and critical-current noise are written as

$$\Gamma_{f,\Phi} = A_1 \left(\frac{\partial \omega_r}{\partial \Phi_{\text{ext}}} \right), \quad \Gamma_{f,I} = A_2 \left(\frac{\partial \omega_r}{\partial I_c} \right), \quad (\text{B26})$$

respectively. In the following discussions, we evaluate the decoherence effects induced by these bias noises.

4. Multi-SQUID-terminated resonator

As shown in Fig. 7, the one-dimensional TLR can also be terminated at its right side by a series of N dc SQUIDs [56,61]. Each SQUID can be tuned by via an independent external flux bias. The two Josephson junctions of the j th SQUID are symmetric with identical Josephson energy E_{sj} and capacitance C_{sj} . The effective Josephson energy is tuned with the external flux $\Phi_{\text{ext},j}$ according to the relation $E_j = 2E_{sj} \cos(\pi \Phi_{\text{ext},j} / \Phi_0)$, and the nonlinear inductance is given by $L_{sj}(\Phi_{\text{ext},j}) = \Phi_0^2 / (2\pi)^2 E_j$. The Lagrangian of the j th SQUID is

$$\mathcal{L}_j = \sum_{i=1,2} \left[\frac{\Phi_0^2}{2(2\pi)^2} C_{sj} (\dot{\phi}_{ji})^2 - E_{sj} \cos \phi_{ji} \right], \quad (\text{B27})$$

where ϕ_{ji} is the phase difference of the i th junction in the j th SQUID. Similarly to the single SQUID case, we obtain the boundary equation at the right-hand side of Eq. (B9) [56]:

$$\psi(d_0, t) = \sum_j^N \phi_{j+}(t), \quad (\text{B28a})$$

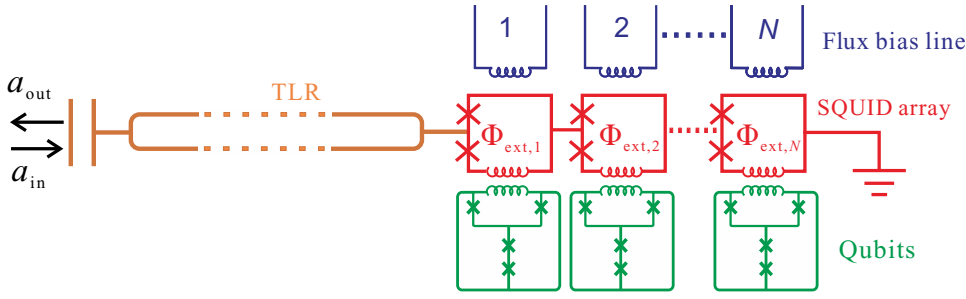


FIG. 7. A quarter-wavelength TLR terminated by an array of N SQUIDs. The effective nonlinear inductance of the j th SQUID is controlled via the external flux $\Phi_{\text{ext},j}$, which contains a static part (produced by the j th bias line) and a perturbation part (produced by the circulating current of the j th flux qubit).

$$2C_s\ddot{\psi}(d_0, t) + \frac{(2\pi)^2}{\Phi_0^2} E_j(\Phi_{\text{ext},j})\phi_{j+}(t) + \frac{\partial_x \psi(d_0, t)}{L_0} = 0, \quad (\text{B28b})$$

where $\phi_{j+} = (\phi_{j1} + \phi_{j2})/2$. By expanding the left-hand side of Eq. (B28b) with ω_r/ω_0 around $\pi/2$ to first order, we obtain

$$\omega_r = \omega_0 \left[1 - \frac{\sum_j^N L_{sj}(\Phi_{\text{ext},j})}{L_t} \right], \quad (\text{B29})$$

from which we can find that the external flux $\Phi_{\text{ext},j}$ through the j th SQUID determines its nonlinear inductance independently. Their joint effect eventually shifts the mode frequency to ω_r . Similarly to the discussions of the single-SQUID case, we obtain the resonator frequency ω_{r0} and the flux sensitivity R_j of the j th SQUID as

$$\omega_{r0} = \omega_0 \left[1 - \sum_{j=1}^N \frac{L_s(\Phi_{\text{ext},j}^0)}{L_t} \right], \quad (\text{B30a})$$

$$R_j = \left. \frac{\partial \omega_r}{\partial \Phi_{\text{ext},j}} \right|_{\Phi_{\text{ext},j}^0} = -\frac{\pi \omega_0 L_s(\Phi_{\text{ext},j}^0)}{\Phi_0 L_t} \tan\left(\frac{\pi \Phi_{\text{ext},j}^0}{\Phi_0}\right). \quad (\text{B30b})$$

The above discussions can also be applied to the single-SQUID case by setting $N = 1$. Assuming that the flux perturbations of the j th SQUID are produced by the circulating current of a single flux qubit as a quantum bus, then it is possible to dispersively couple multiple qubits with a single resonator. Using this layout, we can achieve a multiqubit QND readout.

APPENDIX C: CIRCULATING CURRENTS IN THE GRADIOMETRIC FLUX QUBIT

As shown in Fig. 8(a), the gap-tunable flux qubit has a gradiometric topology by our adopting an eight-shaped design, and the small α junction is replaced by a SQUID (the α loop). The gradiometric structure splits the persistent current symmetrically. This special geometric arrangement allows one to control the gap value α via the external

flux f_α without disturbing the energy bias [36,38,40]. We assume that the two junctions (with a gauge-invariant phase difference $\varphi_{1,2}$) in the main loop have the same Josephson energy E_J and capacitance C . The other two junctions in the SQUID loop (with a gauge-invariant phase difference $\varphi_{3,4}$) are also identical but with Josephson energies and capacitances smaller by a factor α_0 compared with the junctions in the main loop. Because the loop inductance is usually much smaller than the effective nonlinear junction, we ignore the phase accumulated along each loop circumference. Therefore, the fluxoid quantization conditions of the $f_\alpha, f_{\epsilon 1}$, and $f_{\epsilon 2}$ loops are [39,49]

$$\varphi_3 - \varphi_4 + 2\pi f_\alpha = 2\pi N_\alpha, \quad (\text{C1a})$$

$$\varphi_3 + \varphi_1 + \varphi_2 + 2\pi f_{\epsilon 1} = 2\pi N_{\epsilon 1}, \quad (\text{C1b})$$

$$-\varphi_4 - \varphi_1 - \varphi_2 + 2\pi f_{\epsilon 2} = 2\pi N_{\epsilon 2}, \quad (\text{C1c})$$

where $N_\alpha, N_{\epsilon 1}$, and $N_{\epsilon 2}$ are the integer numbers of the trapped fluxoids, and $f_\alpha = \Phi_\alpha/\Phi_0$, $f_{\epsilon 1} = \Phi_{\epsilon 1}/\Phi_0$, and $f_{\epsilon 2} = \Phi_{\epsilon 2}/\Phi_0$, with Φ_α ($\Phi_{\epsilon 1}, \Phi_{\epsilon 2}$) being the external flux through the f_α ($f_{\epsilon 1}, f_{\epsilon 2}$) loop. We assume $N_\alpha = 0$. By our setting $n = N_{\epsilon 2} - N_{\epsilon 1}$ and $f_\epsilon = \Phi_\epsilon/\Phi_0 = f_{\epsilon 1} - f_{\epsilon 2}$, the above boundary conditions reduce the freedom of the systems and thus $\varphi_{3,4}$ and can be given in terms of φ_1 and φ_2

$$\varphi_{3,4} = -\pi(n + f_\epsilon) - (\varphi_1 + \varphi_2) \mp \pi f_\alpha. \quad (\text{C2})$$

The Josephson energy (or the potential energy) for this four-junction system as a function of φ_1 and φ_2 is expressed as

$$U/E_J = 2 + 2\alpha_0 - \cos \varphi_1 - \cos \varphi_2 - 2\alpha_0 \cos(\pi f_\alpha) \cos[\varphi_1 + \varphi_2 + \pi(n + f_\epsilon)]. \quad (\text{C3})$$

We now consider the charging energy stored in the capacitances of the four junctions in this circuit, and the kinetic energy has the form

$$T = \frac{1}{2} \left(\frac{\Phi_0}{2\pi} \right)^2 \sum_{i=1}^4 C_i \dot{\varphi}_i^2 = \left(\frac{\Phi_0}{2\pi} \right)^2 C \left[\frac{(1 + 2\alpha_0)}{4} (\dot{\varphi}_1^2 + \dot{\varphi}_2^2) + \alpha_0 \dot{\varphi}_1 \dot{\varphi}_2 \right], \quad (\text{C4})$$

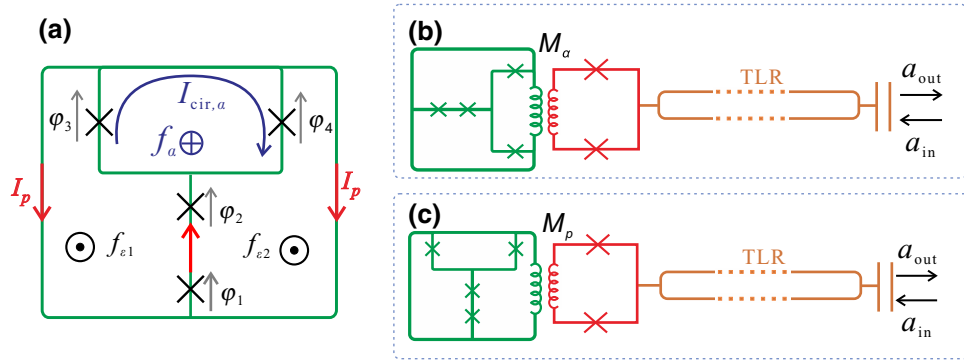


FIG. 8. (a) A gradiometric flux qubit. The Josephson junctions are represented by the crosses. The phase difference across the i th junction is denoted by φ_i . The energy bias (energy gap) of the flux qubit is controlled via the reduced magnetic flux $f_{\epsilon 1(2)} = \Phi_{\epsilon 1(2)}/\Phi_0$ ($f_\alpha = \Phi_\alpha/\Phi_0$) through the two gradiometric loops (α loop). The persistent current I_p (red arrows) is split into two symmetric parts, which circulate around two identical gradiometric loops. Another quantized supercurrent $I_{\text{cir},\alpha}$ circulates in the α loop, which is usually used to create the longitudinal coupling. (b),(c) A flux qubit interacting with a SQUID-terminated resonator via mutual inductance M and circulating current I : (b) M_α and $I_{\text{cir},\alpha}$; (c) M_p and I_p .

where we used the relation $\dot{\varphi}_3 = \dot{\varphi}_4 = -(\dot{\varphi}_1 + \dot{\varphi}_2)$. The Lagrangian for the whole circuit is $\mathcal{L} = T - U$, from which we obtain the canonical momentum $p_i = \partial\mathcal{L}/(\partial\dot{\varphi}_i)$ as the conjugate to the coordinate φ_i . Therefore, by using a Legendre transformation, we can write the corresponding Hamiltonian as

$$\begin{aligned}
 H &= \sum_{i=1,2} p_i \dot{\varphi}_i - \mathcal{L} \\
 &= \frac{4E_c}{1+4\alpha_0} [(1+2\alpha_0)(p_1^2 + p_2^2) - 4\alpha_0 p_1 p_2] \\
 &\quad + E_J \left\{ 2 + 2\alpha_0 - \cos\varphi_1 - \cos\varphi_2 \right. \\
 &\quad \left. - 2\alpha_0 \cos(\pi f_\alpha) \cos[\varphi_1 + \varphi_2 + \pi(n + f_\epsilon)] \right\}. \quad (\text{C5})
 \end{aligned}$$

To quantize the above Hamiltonian, we introduce the commutation relation $[\varphi_i, p_j] = i\delta_{ij}$ with $p_i = -i\partial/\partial\varphi_i$.

For a flux qubit, to minimize the dephasing induced by the flux noise in the main loop, one usually operates the flux qubit at its degeneracy point with $f_\epsilon = 0$. Moreover, under the condition $0 < 2\alpha_0 \cos\pi f_\alpha < 1$, the potential U has a double-well shape. The eigenproblem described by Eq. (C5) can be numerically solved in the plane-wave basis [46]. As discussed in Ref. [39], the two lowest energy levels are well separated from all the higher ones. The ground state $|g\rangle$ and the first excited state $|e\rangle$ are, respectively, symmetric and antisymmetric along the axis $\varphi_+ = \varphi_1 + \varphi_2$, and can be approximately expressed as [49]

$$|g\rangle = \frac{1}{\sqrt{2}}(|+I_p\rangle + |-I_p\rangle), \quad (\text{C6a})$$

$$|e\rangle = \frac{1}{\sqrt{2}}(|+I_p\rangle - |-I_p\rangle), \quad (\text{C6b})$$

where $|\pm I_p\rangle$ are the two persistent-current states of the opposite directions in the main loop [45,46]. To calculate the circulating current in the α loop, we focus our attention on the supercurrent through junctions 3 and 4, which is expressed as

$$I_{3,4} = \frac{2\pi\alpha_0 E_J}{\Phi_0} \sin\varphi_{3,4} = I_c \sin\varphi_{3,4}. \quad (\text{C7})$$

Using the relation in Eq. (C2) and expanding $I_{3(4)}$ in the basis of $|g\rangle$ and $|e\rangle$, we obtain the current operator for junctions 3 and 4 as follows:

$$\begin{aligned}
 I_{3(4)} &= \begin{pmatrix} I_{3(4),ee} & I_{3(4),eg} \\ I_{3(4),ge} & I_{3(4),gg} \end{pmatrix} \\
 &= I_c \begin{pmatrix} \langle e|\sin(\varphi_+ \pm \pi f_\alpha)|e\rangle & \langle e|\sin(\varphi_+ \pm \pi f_\alpha)|g\rangle \\ \langle g|\sin(\varphi_+ \pm \pi f_\alpha)|e\rangle & \langle g|\sin(\varphi_+ \pm \pi f_\alpha)|g\rangle \end{pmatrix}. \quad (\text{C8})
 \end{aligned}$$

Because $|g\rangle$ ($|e\rangle$) is of even (odd) parity with respect to φ_+ at the degeneracy point, it is easy to verify that

$$I_{3,ii} = -I_{4,ii} = \sin(\pi f_\alpha) I_c \langle i|\cos(\varphi_+)|i\rangle \quad (\text{C9})$$

for $i = e, g$. Therefore, given that the qubit is in its excited (ground) state, the average currents of junctions 3 and 4 are of opposite sign, and they generate a circulating current with amplitude $I_{3,ee}$ ($I_{3,gg}$) in the α loop. For the off-diagonal terms, it can be easily verified that

$$I_{3,eg} = I_{4,eg} = \cos(\pi f_\alpha) I_c \langle e|\sin(\varphi_+)|g\rangle, \quad (\text{C10})$$

which is, in fact, equal to the persistent-current I_p of the main loop (related to the σ_x operator). Therefore, the circulating-current operator in the α loop and the

persistent-current operator in the main loop are expressed as

$$I_{\text{cir},\alpha} = \frac{I_3 - I_4}{2} = I_+ I_0 + I_- \sigma_z, \quad (\text{C11a})$$

$$I'_p = I_3 + I_4 = 2I_{3,eg} (|e\rangle\langle g| + |g\rangle\langle e|) = I'_p \sigma_x, \quad (\text{C11b})$$

where

$$I_+ = (I_{3,ee} + I_{3,gg})/2, \quad I_- = (I_{3,ee} - I_{3,gg})/2,$$

and I_0 is the identity operator. The standard definition of the SQUID circulating current in Refs. [39,47] also gives the same form for $I_{\text{cir},\alpha}$. From Eq. (C5) we find that the flux qubit is controlled by the external fluxes f_α and f_ϵ . Assuming that $n = 1$ and the flux qubit is prebiased at the optimal point $\{f_\alpha, f_\epsilon\} = \{f_{\alpha 0}, 0\}$, the circulating currents I'_p and $I_{\text{cir},\alpha}$ can also be derived via a thermodynamic relation [39,46]. Specifically, by considering the flux perturbations δf_α and δf_ϵ , we can rewrite the Hamiltonian in Eq. (C5) as

$$H(f_\alpha, f_\epsilon) = H(f_{\alpha 0}, f_{\epsilon 0}) + \frac{\partial H}{\partial f_\alpha} \delta f_\alpha + \frac{\partial H}{\partial f_\epsilon} \delta f_\epsilon. \quad (\text{C12})$$

In the basis of $|e\rangle$ and $|g\rangle$, it can be easily verified that the following thermodynamic relations hold [39,46]:

$$\frac{\partial H}{\partial f_\alpha} = I_{\text{cir},\alpha} \Phi_0; \quad \frac{\partial H}{\partial f_\epsilon} = \frac{I'_p}{2} \Phi_0. \quad (\text{C13})$$

Therefore, we can rewrite Eq. (C12) as

$$H = \frac{1}{2} \omega_q \sigma_z + \frac{I'_p}{2} \sigma_x \delta \Phi_\epsilon + (I_+ I_0 + I_- \sigma_z) \delta \Phi_\alpha, \quad (\text{C14})$$

where $\delta \Phi_\alpha = \delta f_\alpha \Phi_0$, and $\delta \Phi_\epsilon = \delta f_\epsilon \Phi_0$. The circulating currents $I_{\text{cir},\alpha}$ and I'_p obtained from the thermodynamic relation (C13) and the definitions in Eq. (C11b) lead to the same results. For the flux qubit working at its degeneracy point, the qubit transition frequency ω_q between $|e\rangle$ and $|g\rangle$ is determined by the control flux f_α , and the dephasing resulting from the flux noise in f_ϵ vanishes to first order. The effective persistent current circulating in each symmetric main loop is divided by 2 due to the gradiometric topology ($I_p = I'_p/2$).

In this gap-tunable flux qubit, the persistent current I_p of the flux qubit is widely used to create (σ_x -type) dipole couplings. The circulating-current difference I_- in the α loop can be used to induce longitudinal coupling (σ_z type) [40]. As shown in Figs. 8(a) and 8(b), the circulating currents $I_{\text{cir},\alpha}$ and I_p can produce a flux perturbation through the SQUID of the resonator via the mutual inductances M_α and M_p , respectively, which changes the effective length of the

resonator. Specifically, in the basis of $|e\rangle$ and $|g\rangle$, the interaction between $I_{\text{cir},\alpha}$ and the SQUID-terminated resonator corresponds to NPDC.

The circulating currents $I_{\text{cir},\alpha}$ and I_p both naturally enhance the qubit sensitivity to flux noises. The $1/f$ -type flux noise of the α loop leads to the broadening of the qubit transition frequency ω_q , which corresponds to a pure dephasing process (T_2). The flux noise through two gradiometric loops affects the qubit via the persistent-current operator $I_p \sigma_x$, which results in the energy-relaxation process (T_1). Similarly to the discussion in Ref. [91,92,94], the relaxation and dephasing rates can be approximately written as

$$\Gamma_1 = \frac{1}{T_1} \simeq \left(\frac{\partial H}{\partial f_\epsilon} \right)^2 S_\perp(\omega_q) = (I'_p \Phi_0)^2 S_\perp(\omega_q), \quad (\text{C15})$$

$$\Gamma_f = \frac{1}{T_2} \simeq \left(\frac{\partial H}{\partial f_\alpha} \right) A_\alpha = A_\alpha (I_- \Phi_0),$$

where $S_\perp(\omega_q)$ is the noise power at the qubit frequency and A_α is the amplitude of the $1/f$ -type flux noise in the α loop. The nonzero current difference I_- makes the qubit sensitive to the $1/f$ noise in the α loop. As in the following discussion, for the flux qubit, the amplitude of I_- is usually lower than that of the persistent current I_p by about 1 order of magnitude. Moreover, the experimental results reported in Ref. [36] indicate that the flux noise A_α might be much smaller than that of the main loop. Therefore, the dephasing rate induced by I_- is possibly much slower than that in the case when the qubit is operating far away from its optimal point.

APPENDIX D: NUMERICAL RESULTS ON COUPLING STRENGTH, NONLINEARITY, AND DECOHERENCE

We now discuss a set of possible parameters for the SQUID-terminated nonlinear resonator. Our discussions are mainly based on the experimental parameters in Refs. [62,63]. We first consider a $\lambda/4$ resonator with fixed frequency $\omega_0 \simeq 2\pi \times 6$ GHz and total inductance $L_t = 10$ nH. A rapid photon escape rate κ enhances the speed of the qubit readout, and we set $\kappa/2\pi \simeq 16$ MHz in the following discussion. By our assuming $E_{s,0} = 2\pi \times 2.5$ THz, the changes in the flux sensitivity and the self-Kerr-nonlinearity strength with the control flux are shown in Fig. 2. The flux sensitivity $R/2\pi \simeq 16$ MHz/m Φ_0 with Kerr nonlinearity $K_D/2\pi \simeq 110$ kHz at $\Phi_{\text{ext}} \simeq 0.48\Phi_0$.

The flux (critical-current) noise amplitude of the SQUID attached to the resonator can be set as $A_1 = 5 \times 10^{-6} \Phi_0$ ($A_2 = 5 \times 10^{-6} I_c$) [94]. With these values, the dephasing rates in Eq. (B26) are calculated as $\Gamma_{f,\Phi}/2\pi \simeq 75$ kHz and $\Gamma_{f,I}/2\pi \simeq 30$ kHz. Therefore, the reduction of T_2 due to these two dephasing processes can be ignored when compared with κ in our discussions.

To view the whole circuit in Fig. 8(a) as a flux qubit, the effective gap value

$$\alpha' = 2\alpha_0 \cos \pi f_\alpha \quad (\text{D1})$$

should be in the range $0.5 < \alpha' < 1$ [46] so that the double-well potential approximation is valid. In Fig. 9, we plot the changes in the qubit parameters with the external control flux f_α by setting $2\alpha_0 = 1$ [Figs. 9(a), 9(c), and 9(e)] and $2\alpha_0 = 0.75$ [Figs. 9(b), 9(d), and 9(f)], respectively. As shown in Figs. 9(a) and 9(b), the qubit frequency ω_q can be tuned in a wide range when f_α is biased to be nonzero. The slope of ω_q changing with f_α is proportional to the circulating-current difference I_- in the α loop [Eq. (C13)].

As shown in Fig. 9(a), the two-energy-level structure vanishes (i.e., $\omega_q = 0$) at $f_\alpha = 0$ for $2\alpha_0 = 1$. To obtain a qubit energy-level structure, we need to bias f_α far away from zero, for example, to the dashed-line position, where there is an effectively nonzero circulating current $I_- \simeq 60$ nA [Fig. 9(c)]. When we keep on biasing f_α , I_- becomes larger. As described by Eq. (C15), increasing I_- leads to a reduction of the pure dephasing time T_2 . In Fig. 9(e), we find that the pure dephasing time T_2 decreases to about $1 \mu\text{s}$ at the dashed-line position. In a gate operation, one may need a much longer qubit dephasing time. The experimental results in Ref. [36] indicate that the flux noise in the α loop has a much lower amplitude than that in the main loop, and it is possible to obtain greater T_2 in experiments by reducing the $(1/f)$ noise amplitude A_α .

Here we discuss another approach to increase T_2 . If we set $2\alpha_0 < 1$, the qubit is insensitive to the first order of the flux noise in the α loop at $f_\alpha = 0$, and the examples with $2\alpha_0 = 0.75$ are plotted in Figs. 9(b), 9(d), and 9(f). At $f_\alpha = 0$ (point A), the qubit frequency $\omega_q/2\pi \simeq 2$ GHz with $I_- = 0$. Because $I_- = 0$, the qubit is insensitive to first order of the $1/f$ flux noise, and T_2 is much greater than $1 \mu\text{s}$. When this qubit is used for quantum-information processing, one can operate it at point A much a longer dephasing time. Once the qubit state is to be measured, the flux f_α is adiabatically biased away from zero without damping a given qubit state. As shown in Fig. 9(d), the circulating current $I_{\text{cir},\alpha}$ increases with $|f_\alpha|$. At $f_\alpha \simeq 0.22$ (point B), $I_{\text{cir},\alpha} \simeq 50$ nA and the dephasing time $T_2 \sim 1 \mu\text{s}$. As discussed in Ref. [30], the qubit readout can be finished in tens of nanoseconds, and therefore it is possible to perform several measurements within T_2 . After finishing the measurements, one can adiabatically reset the flux bias $f_\alpha = 0$ with a longer dephasing time for further quantum-information processing. When considering the readout via changing the qubit frequency over such a large range, we should reconsider the parameters of the flux qubit carefully (e.g., the transition effects to higher-energy levels, and the degradation of the relaxation time T_1 and the coherence time T_2). The breakdown of the adiabatic approximation,

which indicates coherence loss of the flux qubit, leads to a significantly lower readout fidelity.

As shown in Fig. 8(b), assuming that the qubit interacts with the resonator via mutual inductance M_α , the circulating current $I_{\text{cir},\alpha}$ produces a small deviation part $\delta\Phi_{\text{ext}} = M_\alpha I_{\text{cir},\alpha}$, which can be detected by the resonator with flux sensitivity R . Thus, the flux qubit can be coupled to the SQUID-terminated resonator. To enhance the coupling strength, we should use a large mutual inductance to sense the circulating current. Assuming the mutual inductance between the α loop and the SQUID of the resonator is M_α , the Hamiltonian for the whole system can be written as

$$\begin{aligned} H_D &= \frac{\omega}{2} \sigma_z + \omega_{r0} a^\dagger a \\ &\quad + RM_\alpha (I_+ I_0 + I_- \sigma_z) a^\dagger a + K_D a^\dagger a^\dagger a a \\ &= \frac{\omega}{2} \sigma_z + \omega'_r a^\dagger a + \chi_z^D \sigma_z a^\dagger a + K_D a^\dagger a^\dagger a a, \end{aligned} \quad (\text{D2})$$

where $\chi_z^D = RM_\alpha I_-$ is the NPDC strength and $\omega'_r = \omega_{r0} + RM_\alpha I_+$ is the renormalized mode frequency. One can find that this coupling has no relation to the dipole-field interactions. This qubit readout based on the Hamiltonian (D2) can be denoted as an ‘‘ideal QND measurement’’ because H_D commutes with the qubit operator σ_z .

As depicted in Fig. 9, we set $I_{\text{cir},\alpha} \simeq 60$ nA and $I_p \simeq 300$ nA in our discussion. To obtain strong coupling strengths, we can use the kinetic inductance by sharing a qubit loop branch with the resonator SQUID. The kinetic mutual inductance is about $1 - 3$ pH/ μm , and can be further enhanced by reducing the cross-section area of the wires [39,49,74]. The mutual inductance is about 15 pH with a shared loop length of approximately $5 \mu\text{m}$. Using these parameter values, we find that the coupling strengths are $\chi_z^D \simeq 7$ MHz and $\chi_x^D \simeq 35$ MHz, respectively.

In the readout experiment with the IDC in Ref. [30], the Jaynes-Cummings coupling strength $g_x/2\pi \simeq 90$ MHz with detuning $\Delta_d \simeq 1$ GHz, and the calculated IDC strength $\chi_z^I/2\pi \simeq 8$ MHz with qubit-state-dependent Kerr nonlinearity $K_I/2\pi \simeq 65$ kHz. We find that it is reasonable to assume that $\chi_z^I = \chi_z^D$ and $K_D \simeq K_I$ in our discussions.

Moreover, we plot the change of the energy relaxation time T_1 with f_α . It can be found that T_1 varies over a much smaller scale than T_2 . By our assuming the noise power spectrum at the qubit frequency $S_\perp(\omega_q) = (5 \times 10^{-10})^2 \text{ s}$ [92], the relaxation time $\Gamma_1^{-1} \simeq 9 \mu\text{s}$, which is of the same order as the experimental results [95]. In a qubit-readout proposal based on IDC, the resonator usually has a fast decay rate. By our setting the photon escape rate $\kappa/2\pi = 16$ MHz and $\lambda = 0.1$, the energy relaxation time due to the Purcell effect $T_p = \Gamma_p^{-1}$ is approximately $1 \mu\text{s}$. Because $\Gamma_p \gg \Gamma_1$, it is reasonable to assume that the qubit decay is mainly limited by Purcell effects.

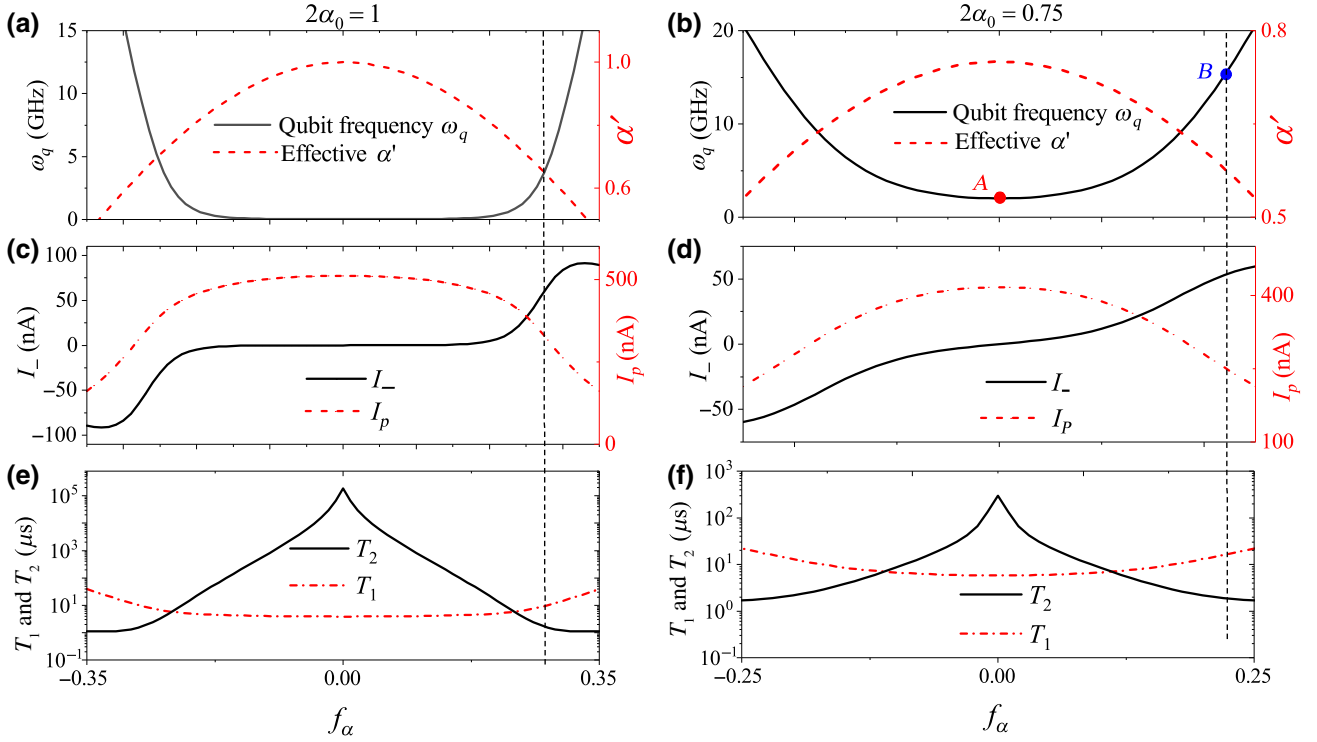


FIG. 9. Flux-qubit parameters versus the external control flux f_α for (a),(c),(e) $2\alpha_0 = 1$ and (b),(d),(f) $2\alpha_0 = 0.75$. These parameters include (a),(b) the effective gap value α' , given in Eq. (D1) (dashed red curve) and the qubit frequency ω_q (solid black curve), (c),(d) circulating-current amplitudes I_- (dashed red curve) and I_p (solid black curve), and (e),(f) the energy-relaxation times T_1 (dash-dotted red curve) and decoherence T_2 (black curve). In (a),(c),(e), the vertical line is at position $f_\alpha \simeq 0.27$. In (b), points A and B correspond to $f_\alpha \simeq 0$ and $f_\alpha \simeq 0.22$, respectively. Here we assume $E_J/2\pi = 320$ GHz and $E_J/E_C = 70$. The flux-noise amplitudes are set as $S_\perp(\omega_q) = 5 \times 10^{-10}$ s and $A_\alpha = 5 \times 10^{-6}$ according to Refs. [92,94].

APPENDIX E: DISPERSIVE QUBIT READOUT WITHOUT PURCELL DECAY

From the discussions above, we find that the Kerr nonlinearity is involved in a qubit readout for both the IDC readout and the NPDC readout. However, these two nonlinearities are due to two different mechanisms: K_D is due to attaching a nonlinear SQUID in the measurement resonator, while K_I results from qubit dressing effects via the dipole-field coupling.

As shown in Fig. 1, at $t = 0$ we apply an incident field a_{in} in the left port at the shifted frequency of the resonator. In the interaction picture, the Langevin equations of the resonator operator, governed by Eq. (A4) (the IDC readout) and Eq. (D2) (the NPDC readout) can, respectively, be written as

$$\begin{aligned} \frac{da(t)}{dt} = & -i\chi_z^I \sigma_z a(t) - 2iK_I \langle n(t) \rangle \sigma_z a(t) \\ & - \frac{1}{2} \kappa a(t) - \sqrt{\kappa} a_{\text{in}}(t), \end{aligned} \quad (\text{E1})$$

$$\frac{da(t)}{dt} = -i\chi_z^D \sigma_z a(t) - 2iK_D \langle n(t) \rangle a(t)$$

$$- \frac{1}{2} \kappa a(t) - \sqrt{\kappa} a_{\text{in}}(t), \quad (\text{E2})$$

where $\langle n(t) \rangle = \langle a^\dagger(t)a(t) \rangle$ is the time-dependent photon number in the resonator. The Kerr term K_I in Eq. (E1) is dependent on the qubit state (i.e., is related to the Pauli operator σ_z), while the Kerr nonlinearity K_D in Eq. (E2) is a standard Kerr term. This input field $a_{\text{in}}(t) = \alpha_{\text{in}} - d_{\text{in}}(t)$ is assumed to be characterized by its mean value (a coherent drive) $\alpha_{\text{in}} = -\epsilon \exp(i\theta_d)/\sqrt{\kappa}$ and a fluctuation part $d_{\text{in}}(t)$. To compare the qubit-readout process for these two different mechanisms, we assume $\chi_z^I = \chi_z^D = \chi_z$ and $K_D = K_I = K$ in the following discussion.

Below we start from the ideal readout without the Kerr nonlinearity (i.e., $K = 0$) and give an analytical form for the measurement fidelity. Then we reconsider the nonlinear effects in these two cases.

1. Ideal readout: measurement without Kerr nonlinearity

By setting $K_D = K_I = K = 0$, we obtain the same linear Langevin differential equation from both Eq. (E1) and Eq. (E2). The average part of the output field is obtained from

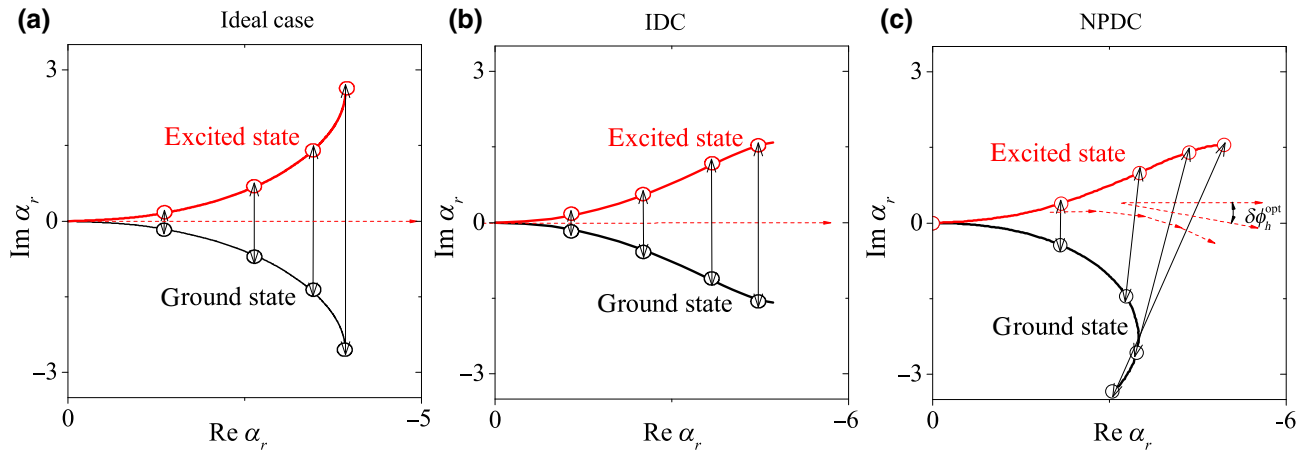


FIG. 10. Evolution in phase space of the intracavity field for the (a) ideal [(Eq. E4)], (b) IDC [(Eq. E1)], and (c) NPDC [(Eq. E2)] readouts. The red (black) curves correspond to the qubit being in its excited (ground) state, and the solid black arrows connecting two circles represent the separations between two signals at the same time t . In (c), $\delta\phi_h^{\text{opt}}$ indicates the rotated optimal homodyne angle for a homodyne measurement. In these plots, both Kerr nonlinearity and Purcell effects are considered. The parameters used here are the same as those for Fig. 4(d), and the drive strength is assumed to be the same as for the stop point.

the input-output boundary condition

$$a_{\text{out}} = \sqrt{\kappa}\alpha_r(t) - \epsilon \exp(i\theta_d)/\sqrt{\kappa}, \quad (\text{E3})$$

where $\alpha_r(t)$ is the average field of the resonator, and is derived by our formally integrating the Langevin differential equation [28]:

$$\alpha_r(t) = \frac{\epsilon\sqrt{\kappa} \exp[i(\theta_d - \langle\sigma_z\rangle\theta_q)]}{\sqrt{\frac{1}{4}\kappa^2 + (\chi_z\langle\sigma_z\rangle)^2}} \times \left\{ 1 - \exp\left[-\left(i\chi_z\langle\sigma_z\rangle + \frac{1}{2}\kappa\right)t\right] \right\}, \quad (\text{E4})$$

where $\theta_q = \arctan(2\chi_z/\kappa)$ is the rotation angle of the output field due to the dispersive coupling. The average intracavity photon number is written as in Eq. (12). The output fluctuation part $d_{\text{out}}(\omega)$ in Fourier space can also be obtained from the Langevin differential equation, and is expressed as

$$d_{\text{out}}(\omega) = \left[1 - \frac{\kappa}{i(\omega + \chi_z\langle\sigma_z\rangle) + \frac{1}{2}\kappa} \right] d_{\text{in}}(\omega). \quad (\text{E5})$$

Equation (E5) leads to completely different expressions for different types of input noise $d_{\text{in}}(\omega)$, (e.g., vacuum, single-mode squeezed vacuum, and multimode squeezed vacuum). For simplicity, we assume that $d_{\text{in}}(t)$ is the vacuum without squeezing and that it satisfies the correlation relation $\langle d_{\text{in}}(\omega)d_{\text{in}}^\dagger(\omega') \rangle = \delta(\omega + \omega')$.

Because of the dispersive coupling, the qubit in its ground state or excited state corresponds to rotation of the output field in phase space with two different angles.

The qubit state is encoded in the output quadrature $Y(\phi_h) = a_{\text{out}}^\dagger e^{i\phi_h} + a_{\text{out}} e^{-i\phi_h}$, with ϕ_h being the homodyne-measurement angle. The output signal corresponds to a standard homodyne detection of the quadrature $Y(\phi_h)$, with integration time τ , and has the following form:

$$M(\tau) = \sqrt{\kappa} \int_0^\tau dt \left[a_{\text{out}}^\dagger(t) \exp(i\phi_h) + a_{\text{out}}(t) \exp(-i\phi_h) \right]. \quad (\text{E6})$$

By setting $\langle\sigma_z\rangle = \pm 1$ in Eq. (E4), respectively, one obtains the expression for the separation signal given in Eq. (11). On the other hand, the fluctuations $d_{\text{out}}(t)$ brings noise into the measurement signal. The integrated imprecision noise $M_N(\tau)$ is identical for the qubit ground and excited states, and is expressed as [28]

$$\begin{aligned} M_N^2(\tau) &= [\langle M_N^2(\tau) \rangle_{|e\rangle} + \langle M_N^2(\tau) \rangle_{|g\rangle}] \\ &= 2\kappa \left\{ \int_0^\tau dt [d_{\text{out}}^\dagger(t) e^{i\phi_h} + \text{H.c.}] \right\}^2 = 2\kappa\tau. \quad (\text{E7}) \end{aligned}$$

According to Eq. (11), the signal $M_s(\tau)$ is optimized by setting $\phi_h' = \theta_d - \phi_h = \pi/2$ and $\theta_q = \pi/4$ (i.e., $\chi_z = \kappa/2$) in the long-time limit with $\kappa\tau \gg 1$. In Fig. 10(a), by adopting the same parameters as for Fig. 3(d) (the drive strength is assumed at the stop point), we plot the evolution of the intracavity fields in phase space. The red and black curves represent the qubit in its excited state and ground state, respectively. The two circles connected by the same black arrow correspond to the same time t . We find that the separation direction between these two signals in phase space is along the solid black arrows and is always vertical to the dashed red arrow, which corresponds to the

optimal relative angle $\phi'_h = \theta_d - \phi_h = \pi/2$ of a homodyne measurement. The signal-to-noise-ratio becomes

$$\begin{aligned} \mathcal{R} &= \frac{M_s(\tau)}{M_N(\tau)} \\ &= \frac{2\epsilon\sqrt{2\kappa\tau}}{\kappa} \left[1 - \frac{2}{\kappa\tau} \left(1 - e^{-(1/2)\kappa\tau} \cos \frac{1}{2}\kappa\tau \right) \right]. \end{aligned} \quad (\text{E8})$$

In the following discussion, we discuss the IDC and NPDC readouts. We find that the optimal measurement signal described in Eq. (E8) can be destroyed by both the Kerr effect and the Purcell effects.

2. Kerr nonlinearity for the IDC-based-readout and NPDC-based-readout mechanisms

In the IDC readout, according to the nonlinear Langevin equation (E1), the effective cavity frequency pull $\xi_g(t)$ is reduced by the photon number due to the qubit-dependent Kerr terms, which can be written as

$$\xi_g(t) = -\chi_z - 2Kn_g(t) = -\chi_z \left[1 - \frac{\langle n_g(t) \rangle}{2n_c} \right], \quad (\text{E9})$$

$$\xi_e(t) = \chi_z + 2Kn_e(t) = \chi_z \left[1 - \frac{\langle n_e(t) \rangle}{2n_c} \right], \quad (\text{E10})$$

where $\langle n_g(t) \rangle = \langle a^\dagger(t)a(t) \rangle|_g$ and $\langle n_e(t) \rangle = \langle a^\dagger(t)a(t) \rangle|_e$ are the mean photon numbers when the qubit is in its

ground state and its excited state, respectively. As discussed in Ref. [27], Eq. (E10) indicates that as the measuring photon number is increased, the effective cavity pull ξ is decreased. Specifically, when the intracavity number reaches $\langle n_g(t) \rangle = n_c$ ($\langle n_e(t) \rangle = n_c$), the cavity pull is reduced as $\xi_g(t) = \chi_z/2$ ($\xi_e(t) = \chi_z/2$).

Because the qubit-dependent Kerr nonlinearity is symmetric for the ground and excited states, it can be easily verified that $\langle n_g(t) \rangle \simeq \langle n_e(t) \rangle$ and $\xi_g(t) \simeq -\xi_e(t)$. The reduction of the cavity pull $\xi_{g,e}(t)$ reduces the signal separation in phase space, which can be clearly found by comparing the numerical results in Figs. 10(b) and 10(a). With increasing time t , the separation distances (the black arrows) are significantly reduced compared with those in the ideal readout. Consequently, the required measurement time becomes longer. Therefore, for the IDC readout, increasing the intracavity photon number not only enhances the qubit-error-transition probability (Purcell photon-number limitations) but also reduces the measurement fidelity due to the Kerr nonlinearity K .

For the NPDC readout without the dipole-field coupling, because the intracavity photons do not deteriorate the qubit states, there is no qubit-error transition due to the Purcell effects. However, when $\langle n(t) \rangle$ is large, the Kerr nonlinearity (introduced by the SQUID) induces apparent effects. Differently from the IDC readout, the nonlinearity is not qubit dependent, and the changing of the cavity pull for the two qubit states is not symmetric. For $K < 0$, the cavity pulls for the qubit being in its ground state and its excited state are, respectively,

$$\xi_g(t) = -\chi_z + 2Kn_g(t), \quad \xi_e(t) = \chi_z + 2Kn_e(t), \quad (\text{E11})$$

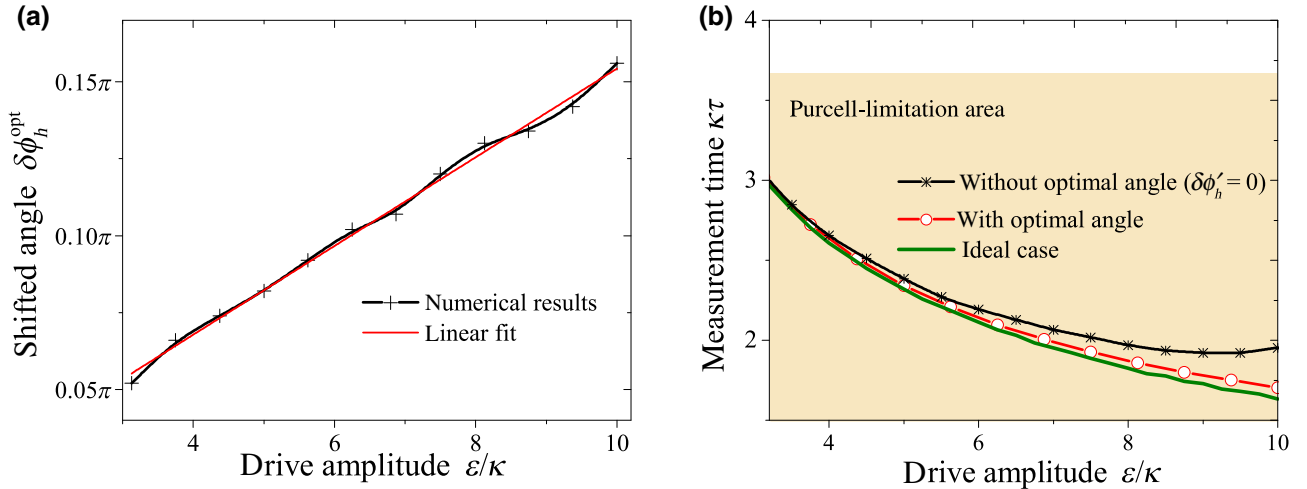


FIG. 11. (a) Optimal shifted homodyne angle $\delta\phi_h^{\text{opt}}$ (corresponding to the shortest measurement time to reach $F = 99.99\%$) versus the drive strength ϵ (in the unit of κ). The curve with crosses shows the numerical results, and the red curves show our linear fit according to the relation $\epsilon/\kappa = a\delta\phi_h^{\text{opt}} + b$. Here we set $a \simeq 0.144$ and $b \simeq 0.01$. (b) Required measurement time to reach fidelity $F = 99.99\%$ for the ideal readout [Eq. (E8)] and for the NPDC readout with and without the optimal shifted angle $\delta\phi_h^{\text{opt}}$. The cyan area corresponds to the Purcell-limitation area. The parameters here are the same as those in Fig. 4.

from which we can find that, by increasing the photon number, the effective cavity pull $|\xi_g|$ ($|\xi_e|$) increases (decreases). This leads to asymmetric rotation angles of the cavity field for the qubit in the ground and excited states, which can be clearly found from Fig. 10(c). The evolutions for the ground and excited states in phase space are asymmetric. The signal-separation direction (black arrows) is now time dependent and rotates in phase space. However, the signal-separation distance is still large compared with the NPDC readout, and is almost equal to that in the ideal readout.

In a homodyne experiment, one can tune the measurement angle ϕ'_h for the NPDC readout to maximize the total signal separation $M_s(\tau)$ during the integration time τ . As sketched in Fig. 10(c), ϕ'_h can be shifted only slightly by an amount $\delta\phi'_h$. For a certain drive strength ϵ , there is an optimal shifted angle $\delta\phi'_h{}^{\text{opt}}$, which corresponds to the shortest measurement time for a certain fidelity. In Fig. 11(a), by adopting the same parameters as for Fig. 3 (with $F = 99.99\%$), we plot the change of $\delta\phi'_h{}^{\text{opt}}$ with ϵ . It can be found that with a stronger drive strength ϵ we need a larger optimal shifted angle $\delta\phi'_h{}^{\text{opt}}$. Their relation can be approximately described by a simple linear function: $\epsilon/\kappa = a\delta\phi'_h{}^{\text{opt}} + b$ (red curve). In Fig. 11(b), we plot the required measurement time to reach fidelity $F = 99.99\%$ for the ideal readout and for the NPDC readout with and without the optimal shifted angle $\delta\phi'_h{}^{\text{opt}}$. We find that even without the optimal shifted angle (curve with asterisks), the measurement can still go into the Purcell-limitation area of the IDC readout (yellow area, below the stop point in Fig. 4). If we choose the optimal shifted angle $\delta\phi'_h{}^{\text{opt}}$, the required time can still be shortened (curve with circles), and it is close to that of the ideal readout case. Therefore, by slight rotation of the measurement angle, the measurement time can go far below the Purcell-limitation area compared with the IDC readout.

[1] D. P. DiVincenzo, Fault-tolerant architectures for superconducting qubits, *Phys. Scr.* **T137**, 014020 (2009).
 [2] S. Ashhab, J. Q. You, and F. Nori, Weak and strong measurement of a qubit using a switching-based detector, *Phys. Rev. A* **79**, 032317 (2009).
 [3] J. Kelly *et al.*, State preservation by repetitive error detection in a superconducting quantum circuit, *Nature (London)* **519**, 66 (2015).
 [4] B. M. Terhal, Quantum error correction for quantum memories, *Rev. Mod. Phys.* **87**, 307 (2015).
 [5] R. Raussendorf and J. Harrington, Fault-Tolerant Quantum Computation with High Threshold in Two Dimensions, *Phys. Rev. Lett.* **98**, 190504 (2007).
 [6] R. Barends *et al.*, Superconducting quantum circuits at the surface code threshold for fault tolerance, *Nature (London)* **508**, 500 (2014).

[7] A. G. Fowler, M. Mariantoni, J. M. Martinis, and A. N. Cleland, Surface codes: Towards practical large-scale quantum computation, *Phys. Rev. A* **86**, 032324 (2012).
 [8] J. Q. You and F. Nori, Quantum information processing with superconducting qubits in a microwave field, *Phys. Rev. B* **68**, 064509 (2003).
 [9] X. Gu, A. F. Kockum, A. Miranowicz, Y.-X. Liu, and F. Nori, Microwave photonics with superconducting quantum circuits, *Phys. Rep.* **718-719**, 1 (2017).
 [10] A. Blais, R.-S. Huang, A. Wallraff, S. M. Girvin, and R. J. Schoelkopf, Cavity quantum electrodynamics for superconducting electrical circuits: An architecture for quantum computation, *Phys. Rev. A* **69**, 062320 (2004).
 [11] F. Mallet, F. R. Ong, A. Palacios-Laloy, F. Nguyen, P. Bertet, D. Vion, and D. Esteve, Single-shot qubit readout in circuit quantum electrodynamics, *Nat. Phys.* **5**, 791 (2009).
 [12] A. F. Kockum, L. Tornberg, and G. Johansson, Undoing measurement-induced dephasing in circuit QED, *Phys. Rev. A* **85**, 052318 (2012).
 [13] S. Gustavsson, O. Zwiier, J. Bylander, F. Yan, F. Yoshihara, Y. Nakamura, T. P. Orlando, and W. D. Oliver, Improving Quantum Gate Fidelities by Using a Qubit to Measure Microwave Pulse Distortions, *Phys. Rev. Lett.* **110**, 040502 (2013).
 [14] I. Diniz, E. Dumur, O. Buisson, and A. Auffèves, Ultrafast quantum nondemolition measurements based on a diamond-shaped artificial atom, *Phys. Rev. A* **87**, 033837 (2013).
 [15] A. Wallraff, D. I. Schuster, A. Blais, L. Frunzio, J. Majer, M. H. Devoret, S. M. Girvin, and R. J. Schoelkopf, Approaching Unit Visibility for Control of a Superconducting Qubit with Dispersive Readout, *Phys. Rev. Lett.* **95**, 060501 (2005).
 [16] C. C. Bultink, B. Tarasinski, N. Haandbæk, S. Poletto, N. Haider, D. J. Michalak, A. Bruno, and L. DiCarlo, General method for extracting the quantum efficiency of dispersive qubit readout in circuit QED, *Appl. Phys. Lett.* **112**, 092601 (2018).
 [17] N. Didier, A. Kamal, W. D. Oliver, A. Blais, and A. A. Clerk, Heisenberg-Limited Qubit Read-Out with Two-Mode Squeezed Light, *Phys. Rev. Lett.* **115**, 093604 (2015).
 [18] Y. L. Wu, L. P. Yang, M. Gong, Y. R. Zheng, H. Deng, Z. G. Yan, Y. J. Zhao, K. Q. Huang, A. D. Castellano, W. J. Munro, K. Nemoto, D. N. Zheng, C. P. Sun, Y. X. Liu, X. B. Zhu, and L. Lu, An efficient and compact switch for quantum circuits, *npj Quantum Inf.* **4**, 50 (2018).
 [19] D. Rosenberg, D. Kim, R. Das, D. Yost, S. Gustavsson, D. Hover, P. Krantz, A. Melville, L. Racz, G. O. Samach, S. J. Weber, F. Yan, J. L. Yoder, A. J. Kerman, and W. D. Oliver, 3D integrated superconducting qubits, *npj Quantum Inf.* **3**, 42 (2017).
 [20] F. Yan, P. Krantz, Y. Sung, M. Kjaergaard, D. L. Campbell, T. P. Orlando, S. Gustavsson, and W. D. Oliver, Tunable Coupling Scheme for Implementing High-Fidelity Two-Qubit Gates, *Phys. Rev. Appl.* **10**, 054062 (2018).
 [21] J. Goetz, F. Deppe, K. G. Fedorov, P. Eder, M. Fischer, S. Pogorzalek, E. Xie, A. Marx, and R. Gross, Parity-Engineered Light-Matter Interaction, *Phys. Rev. Lett.* **121**, 060503 (2018).

- [22] J.-L. Orgiazzi, C. Deng, D. Layden, R. Marchildon, F. Kita-
pli, F. Shen, M. Bal, F. R. Ong, and A. Lupascu, Flux
qubits in a planar circuit quantum electrodynamics archi-
tecture: Quantum control and decoherence, *Phys. Rev. B*
93, 104518 (2016).
- [23] J. T. Peltonen, P. C. J. J. Coumou, Z. H. Peng, T. M.
Klapwijk, J. S. Tsai, and O. V. Astafiev, Hybrid rf SQUID
qubit based on high kinetic inductance, *Sci. Rep.* **8**, 10033
(2018).
- [24] F. Armata, G. Calajo, T. Jaako, M. S. Kim, and P. Rabl, Har-
vesting Multiqubit Entanglement from Ultrastrong Interac-
tions in Circuit Quantum Electrodynamics, *Phys. Rev. Lett.*
119, 183602 (2017).
- [25] M. Boissonneault, J. M. Gambetta, and A. Blais, Nonlinear
dispersive regime of cavity QED: The dressed dephasing
model, *Phys. Rev. A* **77**, 060305 (2008).
- [26] D. Zueco, G. M. Reuther, S. Kohler, and P. Hänggi, Qubit-
oscillator dynamics in the dispersive regime: Analytical
theory beyond the rotating-wave approximation, *Phys. Rev.*
A **80**, 033846 (2009).
- [27] M. Boissonneault, J. M. Gambetta, and A. Blais, Dispersive
regime of circuit QED: Photon-dependent qubit dephasing
and relaxation rates, *Phys. Rev. A* **79**, 013819 (2009).
- [28] N. Didier, J. Bourassa, and A. Blais, Fast Quantum Non-
demolition Readout by Parametric Modulation of Longi-
tudinal Qubit-Oscillator Interaction, *Phys. Rev. Lett.* **115**,
203601 (2015).
- [29] A. A. Houck, J. A. Schreier, B. R. Johnson, J. M. Chow,
J. Koch, J. M. Gambetta, D. I. Schuster, L. Frunzio, M. H.
Devoret, S. M. Girvin, and R. J. Schoelkopf, Controlling
the Spontaneous Emission of a Superconducting Transmon
Qubit, *Phys. Rev. Lett.* **101**, 080502 (2008).
- [30] E. Jeffrey, D. Sank, J. Y. Mutus, T. C. White, J. Kelly,
R. Barends, Y. Chen, Z. Chen, B. Chiaro, A. Dunsworth,
A. Megrant, P. J. J. O'Malley, C. Neill, P. Roushan, A.
Vainsencher, J. Wenner, A. N. Cleland, and J. M. Martinis,
Fast Accurate State Measurement with Superconducting
Qubits, *Phys. Rev. Lett.* **112**, 190504 (2014).
- [31] S. De Liberato, Light-Matter Decoupling in the Deep
Strong Coupling Regime: The Breakdown of the Purcell
Effect, *Phys. Rev. Lett.* **112**, 016401 (2014).
- [32] L. C. G. Govia and A. A. Clerk, Enhanced qubit readout
using locally generated squeezing and inbuilt Purcell-decay
suppression, *New J. Phys.* **19**, 023044 (2017).
- [33] J. Aumentado, R. W. Simmonds, B. T. Gard, and K.
Jacobs, Fast, high-fidelity, quantum non-demolition read-
out of a superconducting qubit using a transverse coupling,
arXiv:1809.02597 (2018).
- [34] E. A. Sete, J. M. Martinis, and A. N. Korotkov, Quantum
theory of a bandpass Purcell filter for qubit readout, *Phys.*
Rev. A **92**, 012325 (2015).
- [35] T. Walter, P. Kurpiers, S. Gasparinetti, P. Magnard, A.
Potočnik, Y. Salathé, M. Pechal, M. Mondal, M. Oppliger,
C. Eichler, and A. Wallraff, Rapid High-Fidelity Single-
Shot Dispersive Readout of Superconducting Qubits, *Phys.*
Rev. Appl. **7**, 054020 (2017).
- [36] A. Fedorov, A. K. Feofanov, P. Macha, P. Forn-Díaz, C.
J. P. M. Harmans, and J. E. Mooij, Strong Coupling of a
Quantum Oscillator to a Flux Qubit at its Symmetry Point,
Phys. Rev. Lett. **105**, 060503 (2010).
- [37] J. Q. You, Y.-X. Liu, and F. Nori, Simultaneous Cooling of
an Artificial Atom and its Neighboring Quantum System,
Phys. Rev. Lett. **100**, 047001 (2008).
- [38] F. G. Paauw, A. Fedorov, C. J. P. M. Harmans, and J. E.
Mooij, Tuning the Gap of a Superconducting Flux Qubit,
Phys. Rev. Lett. **102**, 090501 (2009).
- [39] F. G. Paauw, Ph.D. Thesis, Technische Universiteit Delft,
Delft, 2009.
- [40] M. J. Schwarz, J. Goetz, Z. Jiang, T. Niemczyk, F. Deppe,
A. Marx, and R. Gross, Gradiometric flux qubits with a
tunable gap, *New J. Phys.* **15**, 045001 (2013).
- [41] J. Q. You, Y.-X. Liu, C. P. Sun, and F. Nori, Persistent
single-photon production by tunable on-chip micromaser
with a superconducting quantum circuit, *Phys. Rev. B* **75**,
104516 (2007).
- [42] J. Q. You, X. Hu, S. Ashhab, and F. Nori, Low-decoherence
flux qubit, *Phys. Rev. B* **75**, 140515 (2007).
- [43] J. Q. You and F. Nori, Atomic physics and quantum optics
using superconducting circuits, *Nature (London)* **474**, 589
(2011).
- [44] Z. L. Xiang, S. Ashhab, J. Q. You, and F. Nori, Hybrid
quantum circuits: Superconducting circuits interacting
with other quantum systems, *Rev. Mod. Phys.* **85**, 623
(2013).
- [45] J. E. Mooij, T. P. Orlando, L. Levitov, L. Tian, C. H. van
der Wal, and S. Lloyd, Josephson persistent-current qubit,
Science **285**, 1036 (1999).
- [46] T. P. Orlando, J. E. Mooij, L. Tian, C. H. van der Wal,
L. S. Levitov, S. Lloyd, and J. J. Mazo, Superconducting
persistent-current qubit, *Phys. Rev. B* **60**, 15398 (1999).
- [47] Y.-D. Wang, X. B. Zhu, and C. Bruder, Ideal quantum non-
demolition measurement of a flux qubit at variable bias,
Phys. Rev. B **83**, 134504 (2011).
- [48] R. Stassi and F. Nori, Long-lasting quantum memories:
Extending the coherence time of superconducting artificial
atoms in the ultrastrong-coupling regime, *Phys. Rev. A* **97**,
033823 (2018).
- [49] M. J. Schwarz, Ph.D. Thesis, Technische Universität
München, München, 2015.
- [50] N. Lambert, M. Cirio, M. Delbecq, G. Allison, M. Marx, S.
Tarucha, and F. Nori, Amplified and tunable transverse and
longitudinal spin-photon coupling in hybrid circuit-QED,
Phys. Rev. B **97**, 125429 (2018).
- [51] J. E. Johnson, E. M. Hoskinson, C. Macklin, D. H. Slichter,
I. Siddiqi, and J. Clarke, Dispersive readout of a flux
qubit at the single-photon level, *Phys. Rev. B* **84**, 220503
(2011).
- [52] K. Kakuyanagi, S. Kagei, R. Koibuchi, S. Saito, A.
Lupaşcu, K. Semba, and H. Nakano, Experimental analysis
of the measurement strength dependence of superconduct-
ing qubit readout using a Josephson bifurcation readout
method, *New J. Phys.* **15**, 043028 (2013).
- [53] H. Nakano, S. Saito, K. Semba, and H. Takayanagi, Quan-
tum Time Evolution in a Qubit Readout Process with a
Josephson Bifurcation Amplifier, *Phys. Rev. Lett.* **102**,
257003 (2009).
- [54] K. Kakuyanagi, T. Baba, Y. Matsuzaki, H. Nakano, S.
Saito, and K. Semba, Observation of quantum Zeno effect
in a superconducting flux qubit, *New J. Phys.* **17**, 063035
(2015).

- [55] M. Wallquist, V. S. Shumeiko, and G. Wendin, Selective coupling of superconducting charge qubits mediated by a tunable stripline cavity, *Phys. Rev. B* **74**, 224506 (2006).
- [56] M. Sandberg, C. M. Wilson, F. Persson, T. Bauch, G. Johansson, V. Shumeiko, T. Duty, and P. Delsing, Tuning the field in a microwave resonator faster than the photon lifetime, *Appl. Phys. Lett.* **92**, 203501 (2008).
- [57] J. R. Johansson, G. Johansson, C. M. Wilson, and F. Nori, Dynamical Casimir effect in superconducting microwave circuits, *Phys. Rev. A* **82**, 052509 (2010).
- [58] J. R. Johansson, G. Johansson, C. M. Wilson, and F. Nori, Dynamical Casimir Effect in a Superconducting Coplanar Waveguide, *Phys. Rev. Lett.* **103**, 147003 (2009).
- [59] C. M. Wilson, G. Johansson, A. Pourkabirian, M. Simoen, J. R. Johansson, T. Duty, F. Nori, and P. Delsing, Observation of the dynamical Casimir effect in a superconducting circuit, *Nature (London)* **479**, 376 (2011).
- [60] J. R. Johansson, G. Johansson, and F. Nori, Optomechanical-like coupling between superconducting resonators, *Phys. Rev. A* **90**, 053833 (2014).
- [61] C. Eichler and A. Wallraff, Controlling the dynamic range of a josephson parametric amplifier, *EPJ Quantum Technol.* **1**, 1 (2014).
- [62] S. Pogorzalek, K. G. Fedorov, L. Zhong, J. Goetz, F. Wulschner, M. Fischer, P. Eder, E. Xie, K. Inomata, T. Yamamoto, Y. Nakamura, A. Marx, F. Deppe, and R. Gross, Hysteretic Flux Response and Nondegenerate Gain of Flux-Driven Josephson Parametric Amplifiers, *Phys. Rev. Appl.* **8**, 024012 (2017).
- [63] C. Eichler and J. R. Petta, Realizing a Circuit Analog of an Optomechanical System with Longitudinally Coupled Superconducting Resonators, *Phys. Rev. Lett.* **120**, 227702 (2018).
- [64] J. Bourassa, F. Beaudoin, J. M. Gambetta, and A. Blais, Josephson-junction-embedded transmission-line resonators: From Kerr medium to in-line transmon, *Phys. Rev. A* **86**, 013814 (2012).
- [65] S. Richer and D. DiVincenzo, Circuit design implementing longitudinal coupling: A scalable scheme for superconducting qubits, *Phys. Rev. B* **93**, 134501 (2016).
- [66] S. Richer, N. Maleeva, S. T. Skacel, I. M. Pop, and D. DiVincenzo, Inductively shunted transmon qubit with tunable transverse and longitudinal coupling, *Phys. Rev. B* **96**, 174520 (2017).
- [67] P.-M. Billangeon, J. S. Tsai, and Y. Nakamura, Scalable architecture for quantum information processing with superconducting flux qubits based on purely longitudinal interactions, *Phys. Rev. B* **92**, 020509 (2015).
- [68] P.-M. Billangeon, J. S. Tsai, and Y. Nakamura, Circuit-QED-based scalable architectures for quantum information processing with superconducting qubits, *Phys. Rev. B* **91**, 094517 (2015).
- [69] J. Ikonen, J. Goetz, J. Ilves, A. Keränen, A. M. Gunyho, M. Partanen, K. Y. Tan, D. Hazra, L. Grönberg, V. Vesterinen, S. Simbierowicz, J. Hassel, and M. Möttönen, Qubit Measurement by Multichannel Driving, *Phys. Rev. Lett.* **122**, 080503 (2019).
- [70] S. Touzard, A. Kou, N. E. Frattini, V. V. Sivak, S. Puri, A. Grimm, L. Frunzio, S. Shankar, and M. H. Devoret, Gated Conditional Displacement Readout of Superconducting Qubits, *Phys. Rev. Lett.* **122**, 080502 (2019).
- [71] W.-Y. Zhang, K. Kalashnikov, W.-S. Lu, P. Kamenov, T. DiNapoli, and M. E. Gershenson, Microresonators Fabricated from High-kinetic-Inductance Aluminum Films, *Phys. Rev. Appl.* **11**, 011003 (2019).
- [72] L. Grünhaupt, N. Maleeva, S. T. Skacel, M. Calvo, F. Levy-Bertrand, A. V. Ustinov, H. Rotzinger, A. Monfardini, G. Catelani, and I. M. Pop, Loss Mechanisms and Quasiparticle Dynamics in Superconducting Microwave Resonators Made of Thin-Film Granular Aluminum, *Phys. Rev. Lett.* **121**, 117001 (2018).
- [73] David Niepce, Jonathan Burnett, and Jonas Bylander, High Kinetic Inductance NbN Nanowire Superinductors, *Phys. Rev. Appl.* **11**, 044014 (2019).
- [74] R. Meservey and P. M. Tedrow, Measurements of the kinetic inductance of superconducting linear structures, *J. Appl. Phys.* **40**, 2028 (1969).
- [75] A. J. Annunziata, D. F. Santavicca, L. Frunzio, G. Catelani, M. J. Rooks, A. Frydman, and D. E. Prober, Tunable superconducting nanoinductors, *Nanotechnology* **21**, 445202 (2010).
- [76] C. M. Natarajan, M. G. Tanner, and R. H. Hadfield, Superconducting nanowire single-photon detectors: Physics and applications, *Supercond. Sci. Technol.* **25**, 063001 (2012).
- [77] S. Doerner, A. Kuzmin, K. Graf, I. Charaev, S. Wuenesch, and M. Siegel, Compact microwave kinetic inductance nanowire galvanometer for cryogenic detectors at 4.2 K, *J. Phys. Commun.* **2**, 025016 (2018).
- [78] J. Majer, J. M. Chow, J. M. Gambetta, J. Koch, B. R. Johnson, J. A. Schreier, L. Frunzio, D. I. Schuster, A. A. Houck, A. Wallraff, A. Blais, M. H. Devoret, S. M. Girvin, and R. J. Schoelkopf, Coupling superconducting qubits via a cavity bus, *Nature (London)* **449**, 443 (2007).
- [79] M. Grajcar, A. Izmalkov, S. H. W. van der Ploeg, S. Linzen, T. Plecenik, Th Wagner, U. Hübner, E. Il'ichev, H.-G. Meyer, A. Yu. Smirnov, Peter J. Love, Alec Maassen van den Brink, M. H. S. Amin, S. Uchaikin, and A. M. Zagoskin, Four-Qubit Device with Mixed Couplings, *Phys. Rev. Lett.* **96**, 047006 (2006).
- [80] M. Grajcar, A. Izmalkov, S. H. W. van der Ploeg, S. Linzen, E. Il'ichev, Th Wagner, U. Hübner, H.-G. Meyer, Alec Maassen van den Brink, S. Uchaikin, and A. M. Zagoskin, Direct Josephson coupling between superconducting flux qubits, *Phys. Rev. B* **72**, 020503 (2005).
- [81] J. R. Johansson, P. D. Nation, and F. Nori, QuTiP: An open-source Python framework for the dynamics of open quantum systems, *Comput. Phys. Commun.* **183**, 1760 (2012).
- [82] J. R. Johansson, P. D. Nation, and F. Nori, QuTiP 2: A Python framework for the dynamics of open quantum systems, *Comput. Phys. Commun.* **184**, 1234 (2013).
- [83] J. Gambetta, W. A. Braff, A. Wallraff, S. M. Girvin, and R. J. Schoelkopf, Protocols for optimal readout of qubits using a continuous quantum nondemolition measurement, *Phys. Rev. A* **76**, 012325 (2007).
- [84] J. Heinsoo, C. K. Andersen, A. R. S. Krunner, T. Walter, Y. Salathé, S. Gasparinetti, J.-C. Besse, A. Potočnik, A. Wallraff, and C. Eichler, Rapid High-Fidelity Multiplexed Readout of Superconducting Qubits, *Phys. Rev. Appl.* **10**, 034040 (2018).
- [85] J. P. Groen, D. Ristè, L. Tornberg, J. Cramer, P. C. de Groot, T. Picot, G. Johansson, and L. DiCarlo,

- Partial-Measurement Backaction and Nonclassical Weak Values in a Superconducting Circuit, *Phys. Rev. Lett.* **111**, 090506 (2013).
- [86] D. Tan, S. J. Weber, I. Siddiqi, K. Mølmer, and K. W. Murch, Prediction and Retrodiction for a Continuously Monitored Superconducting Qubit, *Phys. Rev. Lett.* **114**, 090403 (2015).
- [87] M. Cirio, K. Debnath, N. Lambert, and F. Nori, Amplified Optomechanical Transduction of Virtual Radiation Pressure, *Phys. Rev. Lett.* **119**, 053601 (2017).
- [88] A. F. Kockum, A. Miranowicz, S. De Liberato, S. Savasta, and F. Nori, Ultrastrong coupling between light and matter, *Nat. Rev. Phys.* **1**, 19 (2018).
- [89] X. Wang, A. Miranowicz, and F. Nori, Ideal quantum nondemolition readout of a flux qubit without Purcell limitations, arXiv:1811.09048 (2018).
- [90] V. Milchakov, L. Planat, É. Dumur, F. Foroughi, J. Puer-tas, S. Leger, K. Bharadwaj, J. Delaforce, C. Naud, W. Hasch-Guichard, J. J. García-Ripoll, N. Roch, O. Buisson, R. Dassonneville, and T. Ramos, Fast high fidelity quantum non-demolition qubit readout via a non-perturbative cross-kerr coupling, arXiv:1905.00271 (2019).
- [91] J. M. Martinis, S. Nam, J. Aumentado, K. M. Lang, and C. Urbina, Decoherence of a superconducting qubit due to bias noise, *Phys. Rev. B* **67**, 094510 (2003).
- [92] G. Ithier, E. Collin, P. Joyez, P. J. Meeson, D. Vion, D. Esteve, F. Chiarello, A. Shnirman, Y. Makhlin, J. Schrieffer, and G. Schön, Decoherence in a supercon-ducting quantum bit circuit, *Phys. Rev. B* **72**, 134519 (2005).
- [93] F. Deppe, M. Mariani, E. P. Menzel, S. Saito, K. Kakuyanagi, H. Tanaka, T. Meno, K. Semba, H. Takayanagi, and R. Gross, Phase coherent dynamics of a superconducting flux qubit with capacitive bias readout, *Phys. Rev. B* **76**, 214503 (2007).
- [94] J. Koch, T. M. Yu, J. Gambetta, A. A. Houck, D. I. Schus-ter, J. Majer, A. Blais, M. H. Devoret, S. M. Girvin, and R. J. Schoelkopf, Charge-insensitive qubit design derived from the Cooper pair box, *Phys. Rev. A* **76**, 042319 (2007).
- [95] M. Stern, G. Catelani, Y. Kubo, C. Grezes, A. Bienfait, D. Vion, D. Esteve, and P. Bertet, Flux Qubits with Long Coherence Times for Hybrid Quantum Circuits, *Phys. Rev. Lett.* **113**, 123601 (2014).